



Three-Dimensional Numerical Analyses of Perpendicular Tunnel Intersections

Filippos Chortis · Michael Kavvadas

Received: 5 July 2020 / Accepted: 28 September 2020 / Published online: 7 October 2020
© Springer Nature Switzerland AG 2020

Abstract This paper investigates the effect of constructing a junction tunnel, intersecting an existing main tunnel at a normal angle, via parametric 3D Finite Element (3D-FE) analyses. The 3D interaction between the tunnels significantly modifies the stress state of the primary support and the surrounding rockmass at the intersection area, compared to that of the single tunnel (quasi plane strain problem), thus making 3D-FE analyses necessary for the realistic design of the primary support at the junction area. The numerical investigation includes deep, circular intersecting tunnels with the junction tunnel excavated, after the main tunnel, via a conventional (non-TBM) method and supported with shotcrete lining. The parametric analyses are performed for a wide range of junction tunnel's diameter, overburden height, in-situ horizontal stress ratio, strength and deformability of the surrounding rockmass. They focus on calculating the axial forces acting on the primary support at the intersection area before, during and after the construction of the junction tunnel. In addition, they identify the extent of the zone influenced by the tunnel interaction. The results of the analyses indicate that the construction of the junction tunnel causes

significant additional compressive loading at the springline of the main tunnel. In contrast, the crown/invert of the opening of the main tunnel is subjected to either compressive loading or unloading (often reaching tensile loading). The results of the analyses are presented in normalized design charts of the axial forces, versus key geomaterial and geometry parameters to facilitate preliminary estimations of primary support requirements at tunnel junctions.

Keywords Tunnel junctions/intersections · Intersection zone · Conventional/SCL tunneling · Breakouts · 3D numerical modeling

1 Introduction

The construction of escape or service cross-passage tunnels is standard practice in the tunnel industry for health and safety (emergency exit), security (emergency access) and functionality (maintenance, storage, etc.). Typical examples are the cross-passage tunnels constructed at every 333 m along the Brenner Base Tunnel in the Alps (Insam et al. 2019). The tunnel junctions are usually constructed at sufficient distance behind the advancing face of the main tunnel to ensure that the excavation of the main tunnel has practically no effect during the construction of the junction tunnel.

F. Chortis (✉) · M. Kavvadas
Department of Geotechnical Engineering, School of Civil Engineering, National Technical University of Athens, Zografou Campus, 9, Iroon Polytechniou Str, 15780 Zografou, Athens, Greece
e-mail: philipposchortis@gmail.com

Analysis of the interaction between the intersecting tunnels and the surrounding rockmass is complicated and requires three-dimensional Finite Element models. During the excavation of the junction tunnel, the surrounding rockmass is subjected to stress redistribution causing additional loading of the main tunnel at the intersection area. If these additional loads exceed the capacity of the primary support of the main tunnel, a potentially unstable zone can develop, leading to structural failures, especially in weak rockmasses and challenging geotechnical conditions. These interaction effects should be taken into account for the safe design of tunnel junctions, particularly in the breakout zone of the main tunnel.

A literature review of the interaction effects on tunnel junctions indicates a lack of analytical closed-form solutions due to the complexity of the problem. Furthermore, as the required 3D-FE analyses are complicated and time-consuming, most relevant numerical investigations study specific problems with results not applicable in other cases. Acknowledging that, the present paper includes a comprehensive set of parametric 3D-FE analyses of tunnel junctions by varying the diameter of the junction tunnel (d), the overburden height (H), the in-situ horizontal stress ratio (K_o), the strength (σ_{cm}) and the deformability (E_m) of the surrounding rockmass and the construction sequence of the junction tunnel (outward or inward excavation at both sides of the main tunnel, either simultaneously or in sequence). The results of the analyses are used to produce general-purpose normalized graphs (design charts) of the axial forces developing in the intersection zone, between the main and the junction tunnel, versus key geomaterial and geometry parameters. These charts can be useful for preliminary estimations of primary support requirements at tunnel junctions.

2 Literature Review

Early studies of tunnel interaction use either experimental approaches of photo-elasticity (Riley 1964; Pant 1971) or computational methods to calculate the stress distribution at tunnel junctions. For instance, Brown and Hocking (1976) and Hocking (1978) carry out 3D Boundary Element (3D-BE) analyses in an infinite, homogeneous, isotropic, linear elastic material to study stress concentration factors at tunnel

junctions for several types of junction geometries (cross “+”, “T”, “H” and “Y”). Gerçek (1986) summarizes the results of these and other early studies and concludes that: intersections are the most structurally vulnerable areas of underground openings leading to potential instability, in-situ stress and intersection configuration and angle significantly influence the interaction effects; thus, the reliable design and support of intersections must consider the 3D nature of the problem.

More recent relevant studies utilize 3D Finite Element or Finite Difference (3D-FE or FD) analyses mainly for the design of specific projects (case studies). Tsuchiyama et al. (1988) conduct elastic numerical analyses and calculate the influence zone at the main tunnel due to the construction of an access tunnel, while Pöttler (1992) performs analyses for a representative tunnel junction configuration in the English Channel Tunnel Project to examine the necessity of increased thickness of the support lining in the vicinity of the intersection zone. Swoboda et al. (1998) use a finite element model to design and evaluate the stability of the intersection between the main and an escape tunnels in the Schönberg Tunnel Project in Austria. Hsiao et al. (2005) and Sjöberg et al. (2006) utilize numerical analyses to examine the behavior of the tunnel intersection areas in the Hsuehshan Tunnel in Taiwan and the Citybanan Tunnel in Stockholm, respectively. Particularly, Hsiao et al. (2005) examine the deformational response of the tunnel junctions and suggest the intersection areas demanding reinforcement via combining numerical analyses and artificial neural networks. Förder et al. (2008) and Schikora et al. (2013) present relevant studies and demonstrate the potential of optimized design by utilizing 3D numerical modeling for tunnel junctions.

Li et al. (2016) use numerical simulations to investigate the deformation, stress and plastic zone of the surrounding material and the internal forces acting on the support lining of a tunnel junction between a subway station tunnel and a construction tunnel at the Shangxinjie Subway Station in Chongqing in China. The results show that the junction tunnel's construction enhances the deformation and plastic zone, mainly at the crown and the sidewalls of the intersection area, and causes stress concentrations at the sidewalls. The calculated extent of the influence zone is either 2.4B or 1.6B, where B is the width of the

junction tunnel, regarding as reference the deformation or stress, respectively. The magnitude of the axial forces in the circumferential and the longitudinal direction is almost equal, while at the crown and invert of the intersection area, the axial forces decrease significantly at almost zero levels. Liu et al. (2017) study the deformational response at the intersection between a major and an adit tunnels at Cheng-Lan Railway in China and conclude to comparable results.

Liu et al. (2009) investigate the interaction effects (distribution of internal forces and deformations) on the primary support measures of perpendicularly intersecting shallow tunnels in the Sydney region by conducting elastoplastic numerical analyses. The construction of both tunnels is simulated as a step-by-step excavation and support sequence. The results indicate that the stress and the deformation field of the support system of the existing tunnel are significantly affected in a zone extending approximately two and a half diameters ($2.5D$) measuring from the center of the intersection. The level of the interaction effects within the influence zone depends on the new tunnel's face advance either to or from the existing tunnel. Specifically, in a region such as Sydney, with a very high horizontal stress regime, the approach of the new tunnel's face towards the existing tunnel causes tensile cracking on the side of the existing tunnel's lining. On the contrary, neither excessive compressive loading nor tensile failure is observed if the new tunnel's face advances away from the existing tunnel.

Jones (2007) studies the distribution of stress in sprayed concrete shallow tunnel junctions and indicates that essential deviations emerge between two- and three-dimensional models simulating tunnel junctions, since 2D modeling, either numerical or analytical, overestimates the factor of safety at the vicinity of the intersection. Furthermore, Jones (2007) discusses the modeling approaches and the response of tunnel junctions, based on both literature data and advanced numerical modeling compared with site measurements of a shaft-tunnel junction. The research concludes that 3D modeling, which incorporates the simulation of the construction sequence, leads to the realistic prediction of stress development at tunnel openings, while simplified analysis methods tend to produce quite unreliable results.

Apart from examining case-studies, some researches study via parametric investigations the loading conditions developing at tunnel junctions. For

instance, Hsiao et al. (2009) conduct parametric 3D-FD analyses and focus on the induced displacements at the intersection between deep tunnels. The results highlight the role of the geological and geotechnical conditions on critical parameters of tunnel junctions (influence zone, areas requiring enhancement, etc.) and point out the necessity of 3D modeling for the adequate design of the support measures, especially if adverse “squeezing” conditions prevail.

Spyridis and Bergmeister (2015) discuss the structural response of the main tunnel if a circular breakout is constructed, due to a perpendicularly intersecting junction tunnel. The research utilizes parametric elastic 3D-FE analyses for shallow tunnels. The excavation and lining installation of the main tunnel is modeled in a single step without precedent deconfinement (wished-in-place), while subsequently, the removal of the breakout is realized, generating the stress redistribution around the opening. The main stress regimes developing on the lining of the intersection area are the following: (i) significant tension at the opening's crown/invert in the longitudinal direction, (ii) very high compression at the opening's springlines in the hoop direction, (iii) potentially considerable tension at the springlines in the longitudinal direction and the crown/invert in the hoop direction, (iv) potentially tension in the main tunnel's lining, further from the opening's boundary, in a diagonal pattern, (left and right from the crown/invert, above and below from the springlines). The zone mostly affected by stress redistribution extends to approximately one diameter ($1d$) of the junction tunnel. Ke et al. (2019) parametrically study the response mechanism and the influencing factors of a shallow subway cross-passage tunnel and result in comparable conclusions.

3 Numerical Models

The present investigation includes parametric 3D numerical analyses with the Simulia Abaqus Finite Element Code. The main and the junction tunnel are assumed to be circular. The diameter of the main tunnel is equal to $D = 12$ m, while the diameter of the junction tunnel is a variable parameter with values equal to $d = 10$ m, 8 m and 6 m (i.e., $D/d = 1.2$, 1.5 and 2). The connection between the primary support linings of the main and the junction tunnel is

monolithic/fully-fixed (full transfer of forces and bending moments).

Figure 1 presents a typical numerical model with $D/d = 1.5$ and highlights some of the definitions used in the present paper. The excavation length for the main tunnel is $L_{exc} = 10D$, while for each branch of the junction tunnel, it is $l_{exc} = 2D$. Benchmark checking has shown that $l_{exc} > 2D$ is not required since it does not influence the magnitude and the distribution of the axial forces developing in the intersection area. Therefore, $l_{exc} = 2D$ is selected, contributing to the reduction of the computational time of the analysis. The basic dimensions (excavation lengths, limits of external boundaries) of the models are constant regardless of the junction tunnel's diameter (d). The overburden height (H), which is a

variable parameter, is simulated by applying to the model constant stress, equal to $p_o = \gamma H$. The models use solid elements for the rockmass and shell elements for the primary support (shotcrete). The rockmass is simulated as a linear elastic-perfectly plastic material following the Generalized Hoek Brown (GHB) failure criterion, as proposed by Kalos and Kavvadas (2017), while the shotcrete is modeled as a linear elastic material.

The models assume that the junction tunnel is constructed after the main tunnel has advanced sufficiently to reach a steady-state. The excavation of the main tunnel is modeled using full-face deconfinement (by applying a reduced internal pressure) along the whole tunnel length, primary support installation and completion of the construction, to

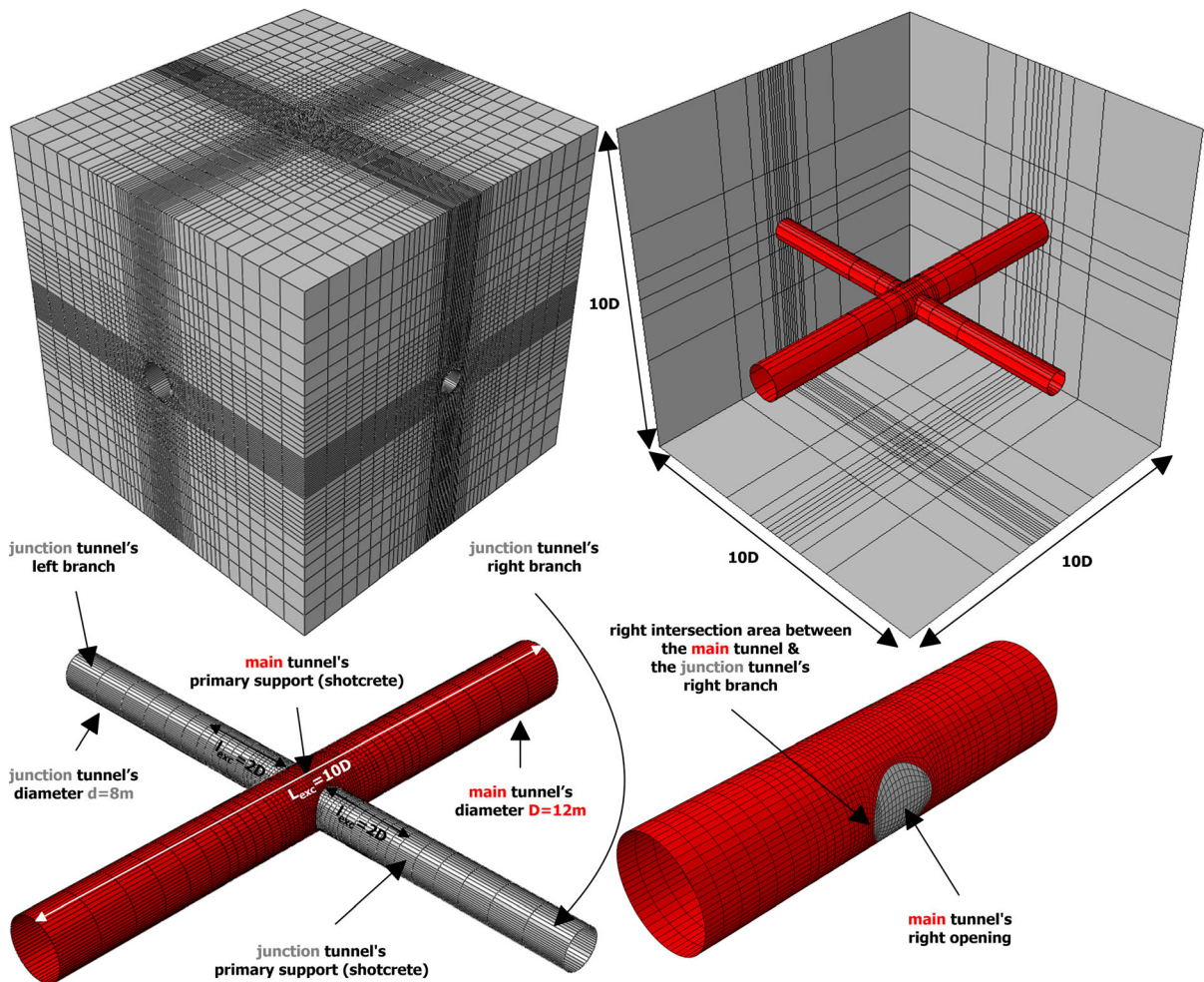


Fig. 1 3D numerical model with $D/d = 1.5$

expedite the analysis. Benchmark checking has shown that this simplification produces practically identical stress and loading conditions compared to a gradual advance of the tunnel excavation front.

On the contrary, the construction of the junction tunnel is modeled via a step-by-step excavation and support sequence according to the principles of conventional/SCL tunneling. This approach produces realistic results of the structural response/interaction between the main and the junction tunnel. The construction sequence of the branches of the junction tunnel (emanating at both sides of the main tunnel) examines the following alternative scenarios:

- scenario 1: simultaneous breakouts (creation of the openings) at both sides of the main tunnel and subsequent outwards excavation in steps of both branches of the junction tunnel (Fig. 2a)

- scenario 2: simultaneous inwards excavation in steps of both branches of the junction tunnel (towards the main tunnel) and subsequent simultaneous breakouts (creation of the openings) at both sides of the main tunnel (Fig. 2b)
- scenario 3: breakout (creation of the opening) at the left side of the main tunnel and subsequent outwards excavation in steps of the left branch of the junction tunnel. Subsequently, application of the same sequence for the right branch of the junction tunnel (Fig. 2c)
- scenario 4: inwards excavation in steps of the left branch of the junction tunnel (towards the main tunnel) and subsequent breakout (creation of the opening) at the left side of the main tunnel. Subsequently, application of the same sequence

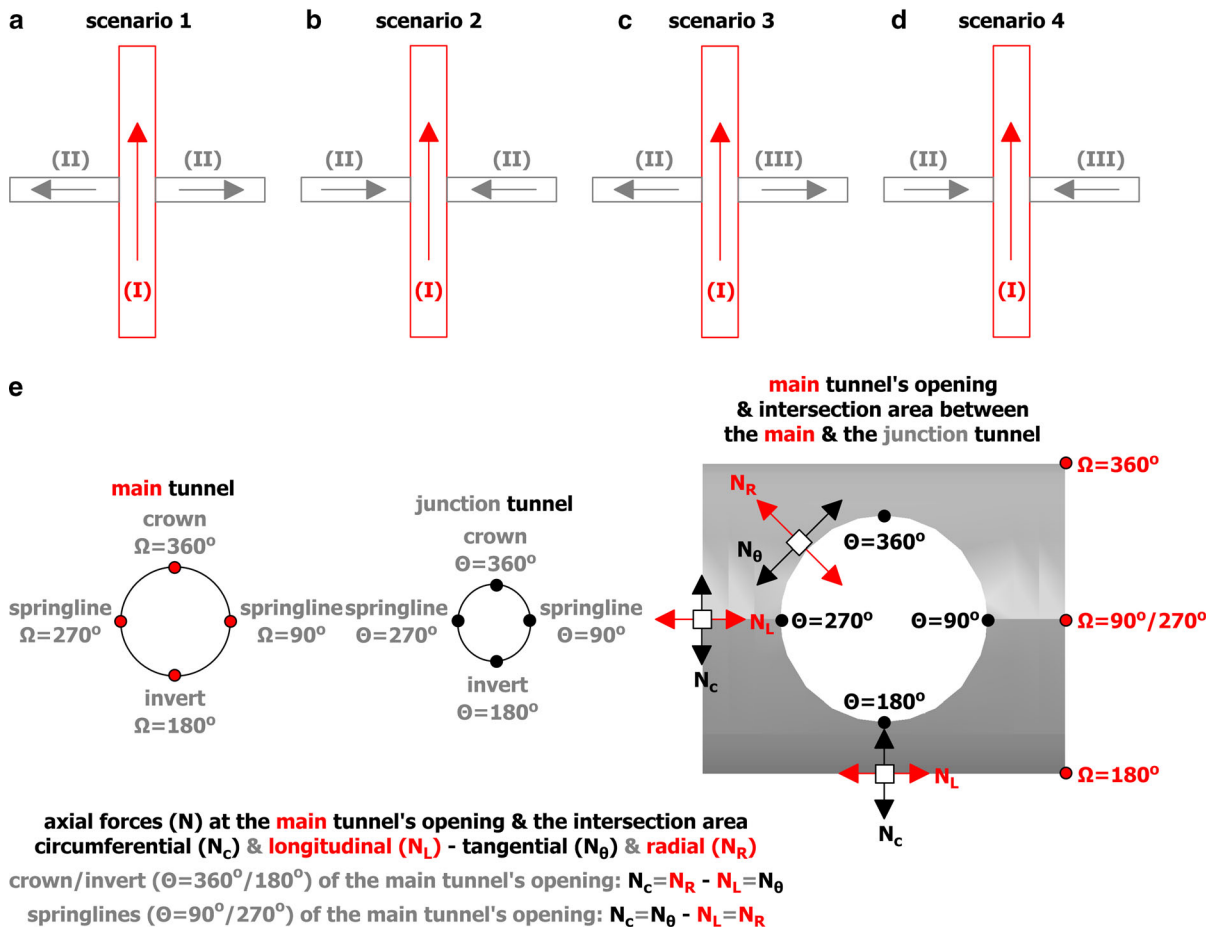


Fig. 2 Assumed construction sequence for each examined scenario (a–d) and orientation of angles (Ω) and (Θ) and axial forces (N) used for presenting results at the periphery of the main tunnel and the periphery of the opening of the main tunnel, respectively (e)

Table 1 Numerical analyses parameters, notations and indicative steps

Category	Parameter	Symbol	Values	Units	
<i>Numerical analyses parameters</i>					
Geometrical parameters	Main tunnel's diameter	D	12	m	
	Junction tunnel's diameter	d	6, 8, 10	m	
	Overburden height ratio	H/D	6.7, 13.4	–	
Geological-geotechnical parameters	Geological strength index (Marinos and Hoek 2018)	GSI	10–50	–	
	UCS of intact rock	σ_{ci}	10–30	MPa	
	Elasticity modulus ratio	MR	350–500	–	
	Elasticity modulus of intact rock	E_i	3500–15000	MPa	
	Constant of Intact Rock	m_i	7–12	–	
	“Global” UCS of rockmass (Hoek and Brown 2019)	σ_{cm}	0.43–5.7	MPa	
	Geotechnical conditions ratio	σ_{cm}/p_o	0.20–2.85	–	
	Elasticity modulus of rockmass (Hoek and Diederichs 2006)	E_m	562–5477	MPa	
	Poisson ratio	ν	0.3	–	
	Unit weight	γ	0.025	MN/ m ³	
		Cohesion	c	0.079–0.664	MPa
		Friction angle	φ	17.5–48.5	deg
		Dilation angle	ψ	4.4–12.1	deg
		In-situ horizontal stress ratio	K_o	0.5, 1, 1.5	–
		Deconfinement ratio	λ	0.5, 0.6, 0.7	–
		Internal pressure ratio	$p_r/p_o = 1 - \lambda$	0.5, 0.4, 0.3	–
	Primary support (shotcrete) parameters	Elasticity modulus	E_{sh}	20000	MPa
Poisson ratio		ν_{sh}	0.2	–	
Thickness		t_{sh}	0.4	m	
Unit weight		γ_{sh}	0.025	MN/ m ³	
<i>Numerical analyses notations</i>					
$p_o = \gamma H$	In-situ stress at the tunnel axis level				
$N/(p_o D)$	Normalized axial force acting on the primary support of the tunnel				
σ_{cm}/p_o	Geotechnical conditions ratio				
$(\sigma_{cm}/p_o)^{0.55} \cdot (H/D)^{0.45}$	Modified geotechnical conditions ratio				
S/R	Normalized longitudinal distance from the center of the intersection area (R: radius of the main tunnel)				
Y/r	Normalized longitudinal distance from the springline of the intersection area (springline of the opening) (r: radius of the junction tunnel)				
JT	Junction tunnel				
MT	Main tunnel				
<i>Numerical analyses indicative steps</i>					
“MT”	Step: primary support installation of the main tunnel				
“Breakout”	Step: breakout (creation of the opening) at the primary support of the main tunnel				
“Breakout_L/_R”	“_L” or “_R” are used to distinguish the left or the right intersection area (or direction)				
“JT”	Step: end of the construction sequence of the junction tunnel				
“JT_L/_R”	“_L” or “_R” are used to distinguish the left or the right intersection area (or direction)				

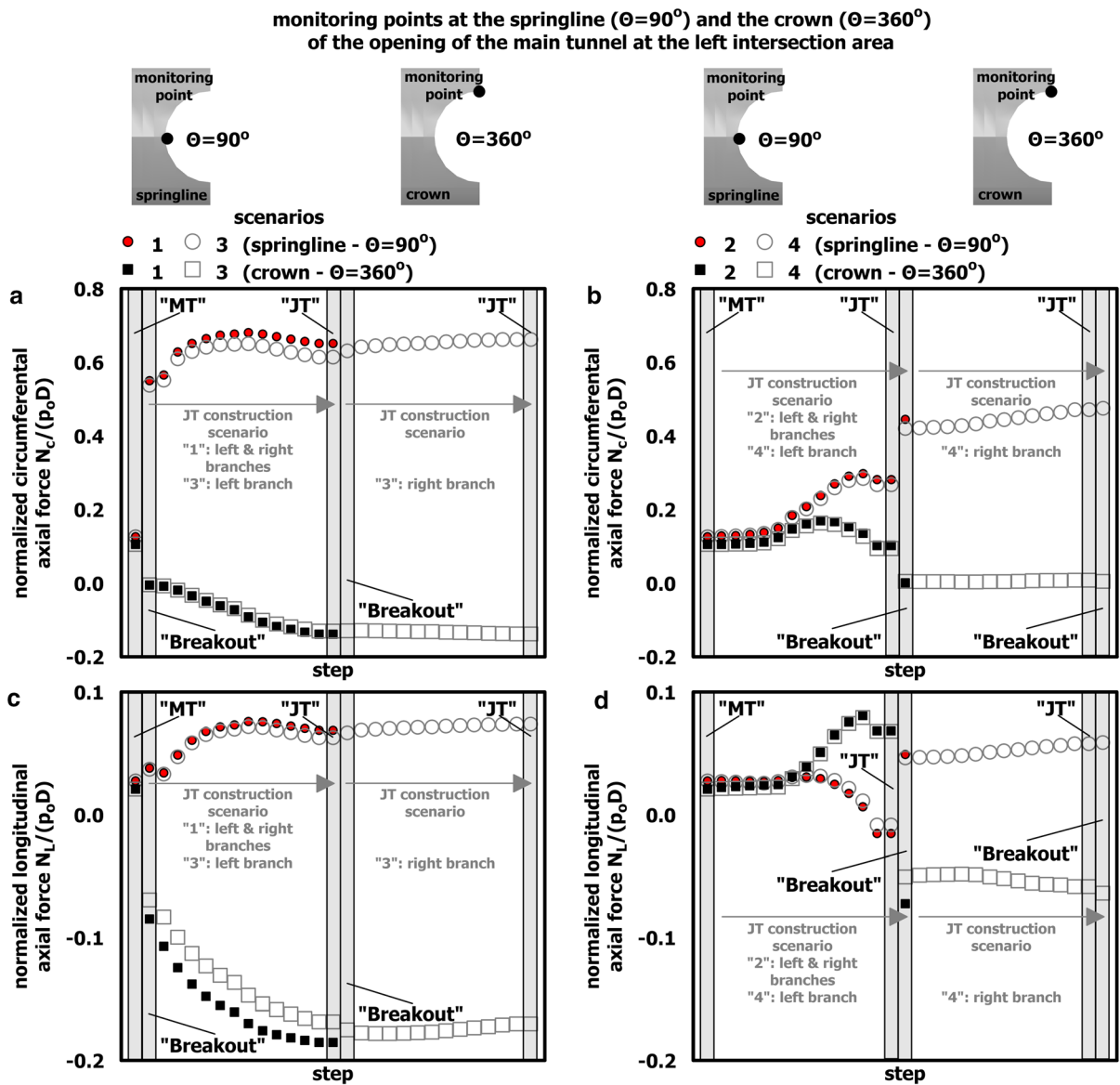


Fig. 3 Evolution of the circumferential (N_c) (a, b) and the longitudinal (N_L) (c, d) axial force at the springline ($\Theta = 90^\circ$) and the crown ($\Theta = 360^\circ$) of the opening of the main tunnel at

the left intersection area, for all examined scenarios 1–4 (Case: $\sigma_{cm}/p_o = 0.4$, $K_o = 0.5$, $H/D = 6.7$, $D/d = 1.5$, $\lambda = 0.7$)

for the right branch of the junction tunnel (Fig. 2d)

Figure 2a–d visualize the mentioned above construction sequence for each examined scenario. The main and the junction tunnel are shown with red and grey colors, respectively. The arrows illustrate the direction of the excavation, while the latin numbers depict the sequence of the excavation. Figure 2e shows the orientation of angles (Ω) and (Θ) and axial

forces (N), used for presenting results at the periphery of the main tunnel and the periphery of the opening of the main tunnel (intersection area between the main and the junction tunnel), respectively. These angles are used in subsequent figures to plot the stress state at the periphery of the breakout zone in each tunnel.

The numerical models correspond to the cross “+” geometry of tunnel junctions (i.e., the branches of the junction tunnel are excavated at both sides of the main

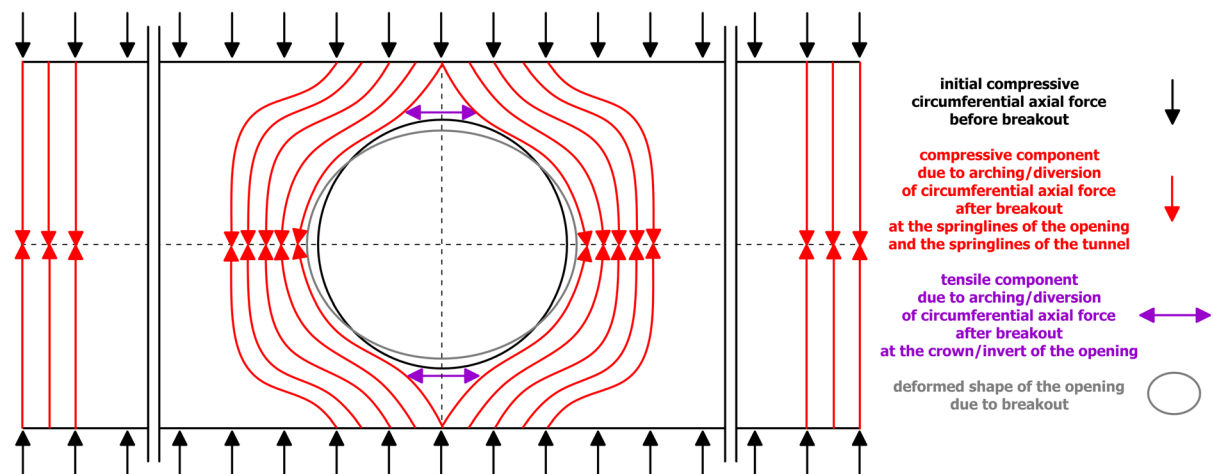


Fig. 4 Simplified schematic (non-scaled) illustration of the redistribution mechanism of the circumferential axial force due to the breakout at the primary support of the main tunnel

tunnel). However, the excavation of each branch of the junction tunnel in sequence (scenarios 3 and 4) incorporates the simulation of “T” configuration and therefore includes the results corresponding to this type of tunnel junctions. Furthermore, taking into account the symmetry between “T” and “H” configurations, the results of the numerical analyses can be used for all three geometries (cross “+”, “T” and “H”).

Table 1 summarizes the values of the examined parameters for the rockmass and the primary support and presents the notations and the indicative steps used within this paper to facilitate the interpretation of the results. In total, 432 parametric 3D numerical analyses have been conducted.

4 Numerical Analyses Results

4.1 Axial Forces Along the Opening—Effect of Scenario (Construction Sequence)

Figure 3 presents the evolution of the circumferential (N_c) (Fig. 3a, b) and the longitudinal (N_L) (Fig. 3c, d) axial force acting on the primary support (shotcrete) at the springline ($\Theta = 90^\circ$) and the crown ($\Theta = 360^\circ$) of the opening of the main tunnel at the left intersection area, during the construction of the junction tunnel, for all examined scenarios. Due to symmetry, the results are identical at the left and right springline and the crown and invert. As discussed subsequently, the

results at the right intersection area are not very different from these at the left one.

The graphs presented in Fig. 3 correspond to adverse geotechnical conditions with low rockmass strength to in-situ stress ratio $\sigma_{cm}/p_o = 0.4$ and high deconfinement ratio $\lambda = 0.7$ during the excavation of the main tunnel. The results of scenarios 1, 3 (Fig. 3a, c) and scenarios 2, 4 (Fig. 3b, d) are similar since they correspond to similar construction sequences (outward and inward excavation of the junction tunnel, respectively). The results of scenario 1 are slightly more adverse to these of the first part of scenario 3, while the second part of scenario 3 produces results comparable to these of scenario 1. This relation is also valid for scenarios 2 and 4.

In scenario 3, the left breakout at the main tunnel’s primary support (first step “Breakout”) is performed shortly after the completion of the construction of the main tunnel (step “MT”). The creation of the opening increases the circumferential compressive axial force at the springline and decreases it, at almost zero levels, at the crown, as presented in Fig. 3a. This response is also reported by Liu et al. (2009), Li et al. (2016), Spyridis and Bergmeister (2015). Subsequently, as shown in Fig. 3a, the advance of the left branch of the junction tunnel increases the compressive axial force at the springline until it stabilizes at the end of its excavation (first step “JT”), while tensile axial force develops at the crown. The right breakout at the main tunnel’s primary support (second step “Breakout”) and the advance of the right branch of the junction

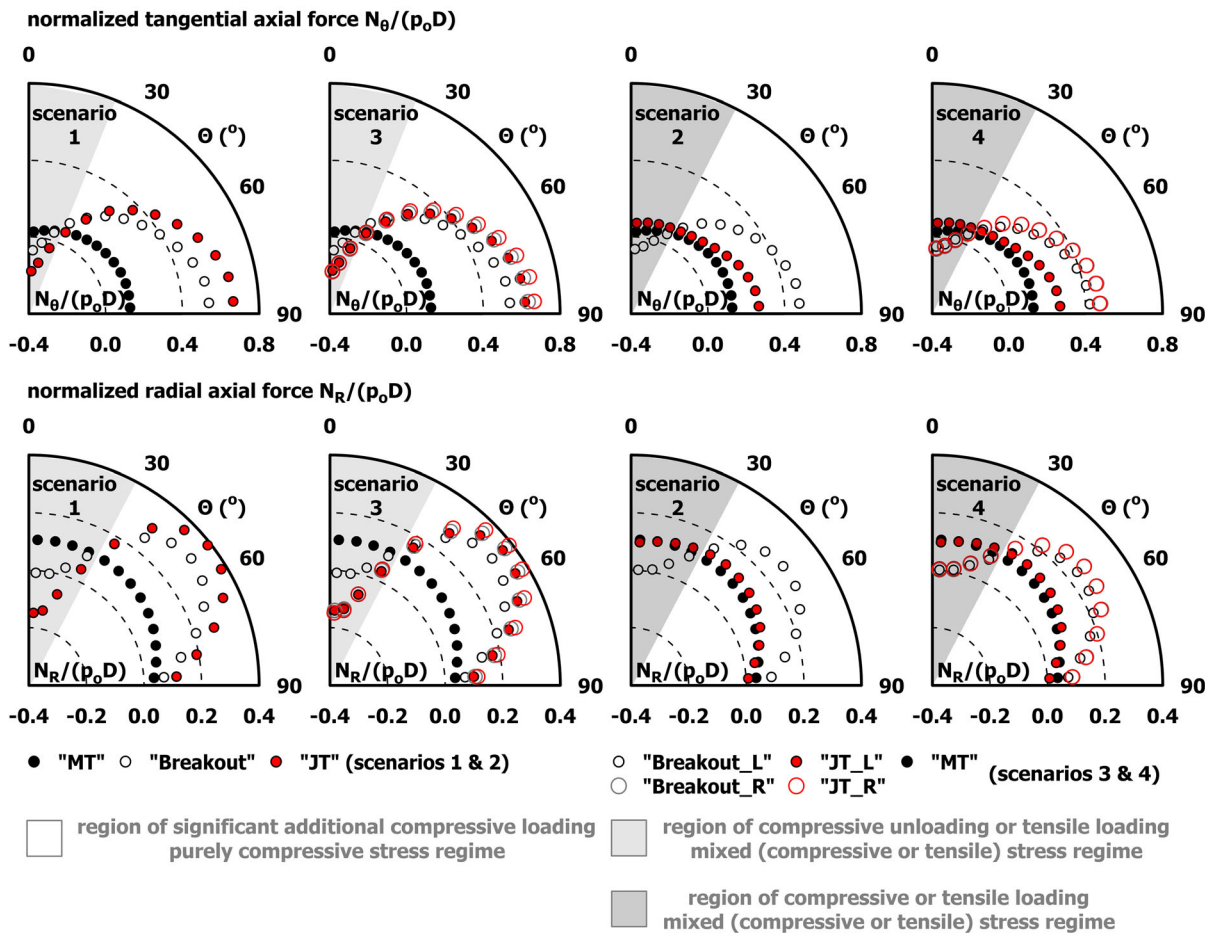


Fig. 5 Distribution of the tangential (N_{θ}) and the radial (N_R) axial force at the periphery of the opening of the main tunnel at the left intersection area, for all examined scenarios 1–4 (Case: $\sigma_{cm}/p_o = 0.4$, $K_o = 0.5$, $H/D = 6.7$, $D/d = 1.5$, $\lambda = 0.7$)

tunnel until the end of its excavation (second step “JT”) slightly increase the compressive stress state at the springline and do not influence the level of the tensile stress state at the crown.

Figure 4 shows a simplified schematic (non-scaled) illustration of the redistribution mechanism of the circumferential axial force due to the creation of the opening at the primary support of the main tunnel. Before the breakout, the initial circumferential axial force (depicted with black color) is vertical and compressive, while after the breakout, stress lines divert around the opening due to arching. As a result of arching, an additional compressive component (depicted with red color) develops at the springline areas of the opening, while a tensile component (depicted with purple color) develops at the crown/invert areas. Therefore, additional compressive loading develops at

the larger part of the periphery of the opening with the maximum effect (maximum compression) exhibiting at the springlines. Respectively, compressive unloading or tensile loading develops at the smaller part of the periphery of the opening with the maximum effect (minimum compression or maximum tension) exhibiting at the crown/invert.

In scenario 4, the construction sequence is reverse: the breakout (step “Breakout”) at each side of the main tunnel’s primary support is realized after the excavation of each branch of the junction tunnel (step “JT”). This differentiation proves to be favorable compared to scenario 3, as presented in Fig. 3b. At the springline, the induced circumferential compressive axial force is lower compared to the corresponding one in scenario 3. At the crown, the developing circumferential axial force is oriented in the margin between

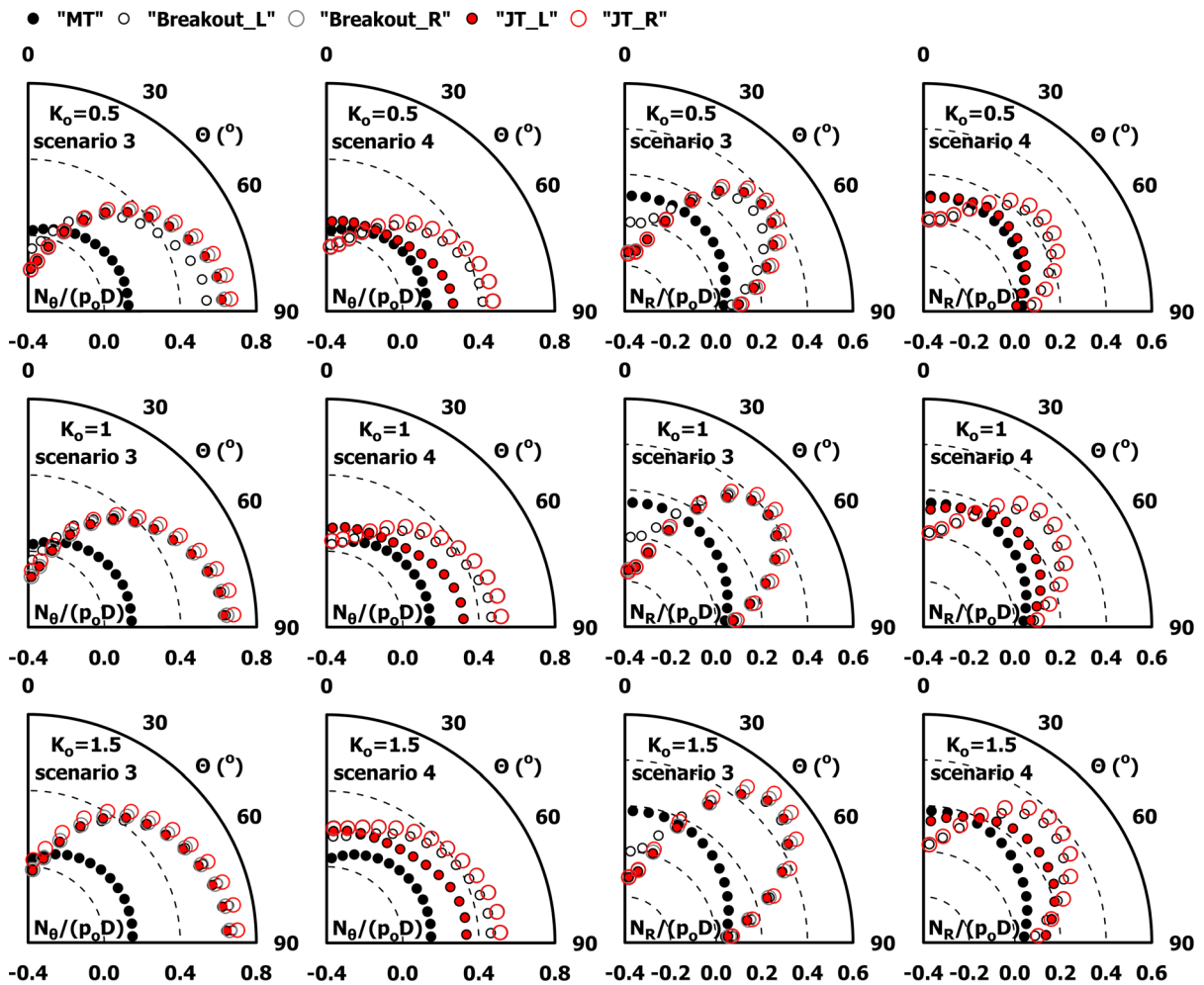


Fig. 6 Distribution of the tangential (N_{θ}) and the radial (N_R) axial force at the periphery of the opening of the main tunnel at the left intersection area, for scenarios 3 and 4 (Case: $\sigma_{cm}/p_o = 0.4$, $K_o = 0.5, 1, 1.5$, $H/D = 6.7$, $D/d = 1.5$, $\lambda = 0.7$)

compression and tension, instead of being tensile as in scenario 3.

In a more detailed analysis of scenario 4, the excavation of the junction tunnel's left branch causes an increasing trend at the circumferential compressive axial force at the springline. This trend depends on the distance from the left intersection area and exhibits its maximum at the left breakout. Concerning the crown, during the excavation of the junction tunnel's left branch, the circumferential axial force is subjected to compressive fluctuations and results to almost zero levels at the breakout. The subsequent excavation of the right branch and the right breakout lead to a slight increase of compression at the springline and do not influence the level of tension at the crown.

In conclusion, two stress patterns prevail at the left intersection area concerning the circumferential axial force (Fig. 3a, b). The first, at the springline, where a stress regime of significant additional loading develops, causing a higher compressive axial force, regardless of the scenario. The second, at the crown, where, depending on the scenario, either a stress regime of unloading generates a tensile axial force (scenario 3) or a mixed stress regime exhibiting a loading (initially) and unloading (finally) trend results to an almost zero axial force (scenario 4).

Figure 3c, d show that, in absolute magnitude, the longitudinal axial force is lower than the circumferential force, at the springline of the opening and approximately of the same level at the crown. In

scenario 3 (Fig. 3c), the formatted patterns and stress regimes are compressive at the springline and tensile at the crown. In scenario 4 (Fig. 3d), the stress regimes of the longitudinal axial force at the springline and the crown initially exhibit transitions between compression and tension and finally stabilize at and after the breakout. The stabilized stress states in scenario 4 are similar to the ones developing in scenario 3 (compressive at the springline and tensile at the crown).

Figure 5 presents the distribution of the tangential (N_θ) and the radial (N_R) axial force acting on the primary support (shotcrete) at the periphery of the opening of the main tunnel at the left intersection area, for all examined scenarios. The tangential and radial axial forces have been calculated by transforming the

circumferential and the longitudinal axial force into polar directions and adding their components in the tangential and the radial direction. Due to the symmetry, the results are shown in the quarter of the periphery ($\Theta = 0^\circ\text{--}90^\circ$). The plots focus on the steps “MT”, “Breakout” and “JT”, as defined in Table 1.

The graphs presented in Fig. 5 indicate in more detail than the plots in Fig. 3 that the results of scenarios 3 and 4 are adequate for the provision of the results of scenarios 1 and 2. In scenarios 3 and 4, two stress regions are identified at the periphery of the opening, due to the construction of the junction tunnel (steps “Breakout_L”, “JT_L”, “Breakout_R”, “JT_R”). The first region ($\Theta = 30^\circ\text{--}90^\circ$) is subjected to significant additional compressive loading,

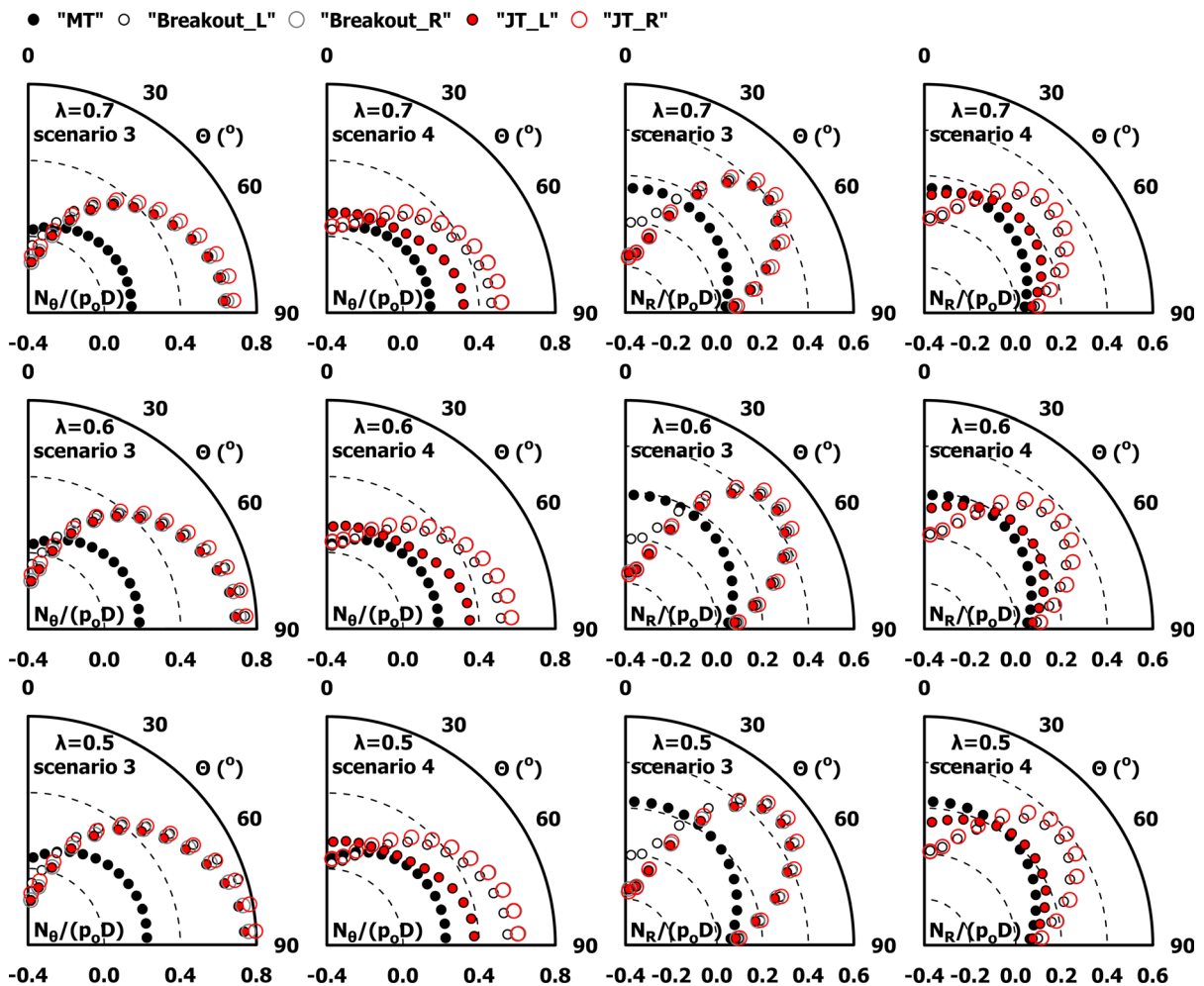


Fig. 7 Distribution of the tangential (N_θ) and the radial (N_R) axial force at the periphery of the opening of the main tunnel at the left intersection area, for scenarios 3 and 4 (Case: $\sigma_{cm}/p_o = 0.4$, $K_o = 1$, $H/D = 6.7$, $D/d = 1.5$, $\lambda = 0.5, 0.6, 0.7$)

regardless of the scenario. The second region ($\Theta = 0^\circ\text{--}30^\circ$) develops either compressive unloading and tensile loading (scenario 3) or compressive and tensile loading (scenario 4). This categorization of the stress regions, noted with a different (color fill) pattern in the graphs, can be adopted for both tangential and radial axial force. Despite the scenario, the tangential axial force exhibits its maximum (compression) at the springline area and minimum (compression or tension) at the crown area. Respectively, the radial axial force maximizes approximately at the bisectrix area (location with $\Theta = 45^\circ$) of the springline and the crown, while it minimizes at the crown area. The results presented in Fig. 5 could serve as an envelope of the induced loading conditions on the periphery of the opening since the distribution of the axial forces is shown at every location of the opening and for indicative steps that include the critical stress states. Thus, these values can contribute to the adequate preliminary design of the primary support's capacity at the intersection area.

4.2 Axial Forces Along the Opening—Effect of K_o , λ and D/d

Figure 6 presents the distribution of the tangential (N_Θ) and the radial (N_R) axial force acting on the primary support at the periphery of the opening of the main tunnel at the left intersection area, for scenarios 3 and 4 and three values of the horizontal stress ratio K_o (0.5, 1 and 1.5). This figure examines the effect of K_o under the limitations that the output corresponds to numerical analyses with specific values for the following parameters σ_{cm}/p_o , H/D , D/d and λ .

The results indicate that the effect of K_o relates to the assumed construction sequence. In this context, for scenario 3, in the tangential direction, the patterns of either developing additional compression at the springline or decreasing compression and leading to tension at the crown are independent of K_o . However, the level of tension at the crown and the subjected to tension opening's region reduce, as K_o increases. Respectively, for scenario 4, the pattern of compressive stress state at the springline is not influenced by K_o , while, at the crown, the stress state is governed by K_o ; the tangential axial force strongly varies from being mixed (compressive and tensile) to entirely compressive according to K_o . Specifically, increasing K_o contributes to limiting or preventing a tensile stress

state at the crown, leading to an entirely compressive stress state at the whole opening's periphery. In the longitudinal direction, K_o has practically no effect on the stress pattern at both the springline and the crown, regardless of the adopted construction sequence.

Concerning the magnitude of the axial forces, increasing K_o leads to a comparatively higher average axial force for the main tunnel (step "MT"). In the radial direction, during and after constructing the junction tunnel (steps "Breakout_L", "JT_L", "Breakout_R", "JT_R"), the axial force is within comparable levels at the crown and the springline, regardless of K_o . However, an increasing trend exhibits, as K_o increases, at the region of the opening oriented for $\Theta = 30^\circ\text{--}60^\circ$, where the radial axial force maximizes. In the tangential direction, at the springline, the axial force is within comparable levels or slightly increases, as K_o increases. At the crown, the magnitude and the sign of the axial force is determined by the combination of K_o and assumed scenario. It is also generally deduced that the loading conditions at the periphery of the opening are more favorable for scenario 4, relative to 3, for every examined value of K_o .

Finally, the reverse stress regime patterns reported by Liu et al. (2009) for $K_o > 1$, thus the developing of tension at the springlines and compression at the crown/invert, is not evaluated within the parametric examination of K_o shown in Fig. 6. The latter is due to the value of K_o assumed by Liu et al. (2009), being much higher than the ones considered in the present paper.

Figure 7 presents the distribution of the tangential (N_Θ) and the radial (N_R) axial force acting on the primary support at the periphery of the opening of the main tunnel at the left intersection area, for scenarios 3 and 4 and three values of the deconfinement ratio λ (0.5, 0.6 and 0.7). This figure examines the effect of λ , indicatively for numerical analyses with specific values for the following parameters σ_{cm}/p_o , K_o , H/D and D/d .

The level of deconfinement is mainly governed by the prevailing geotechnical conditions (mainly rock-mass characteristics and in-situ stress). However, some conventional tunneling actions or parameters (full- or partial-face excavation, face treatment, installation distance of primary support from the tunnel face, advance rate, etc.) could significantly alter its magnitude. Therefore it is parametrically examined

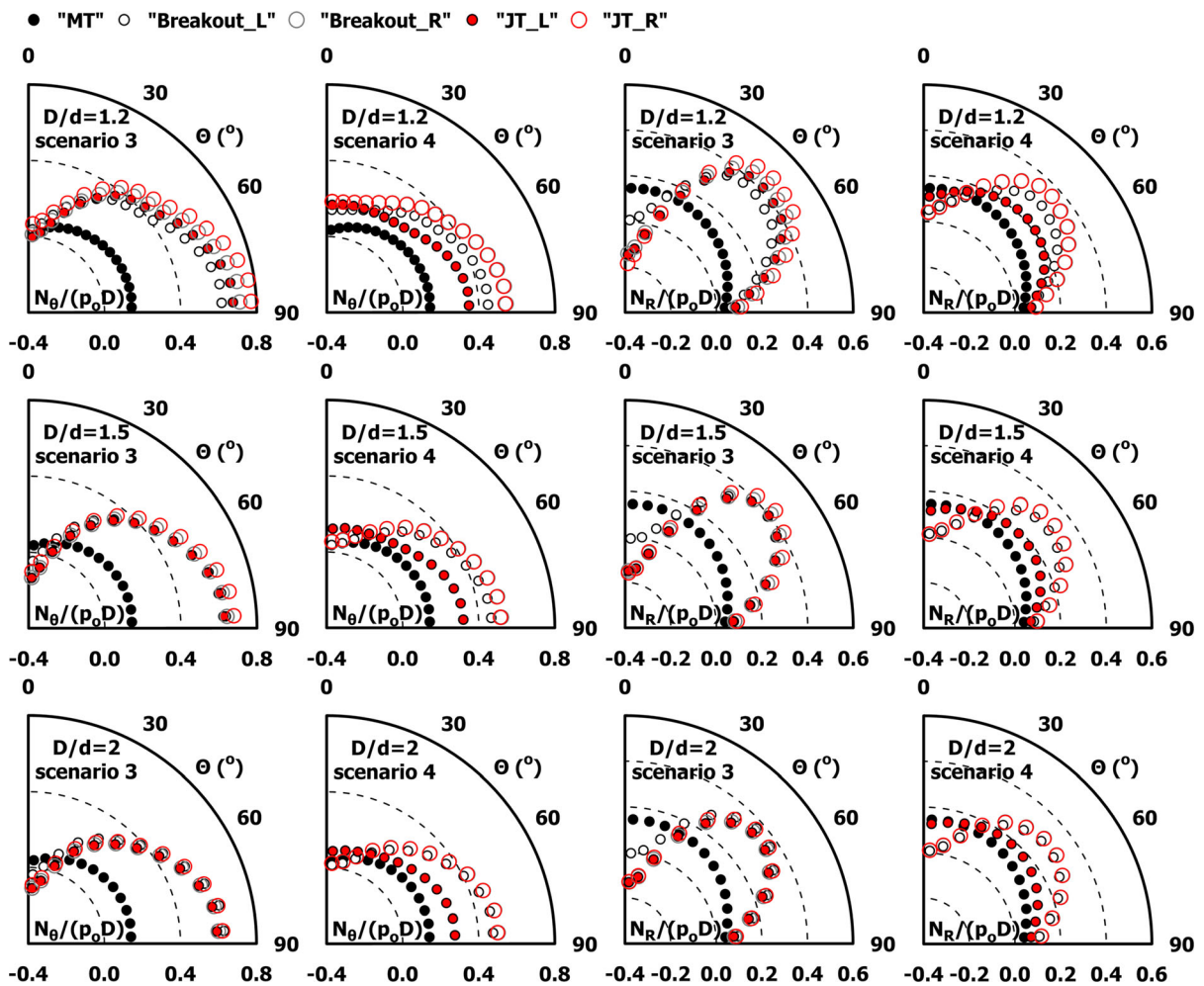


Fig. 8 Distribution of the tangential (N_{θ}) and the radial (N_R) axial force at the periphery of the opening of the main tunnel at the left intersection area, for scenarios 3 and 4 (Case: $\sigma_{cm}/p_0 = 0.4$, $K_o = 1$, $H/D = 6.7$, $D/d = 1.2, 1.5, 2$, $\lambda = 0.7$)

to investigate its effect on the shotcrete layer loading conditions at the intersection area. In the frame of the present paper, the range of the investigated values for λ does not differentiate for either weak or strong rockmass corresponding to lower and higher values for σ_{cm}/p_0 , respectively. For each rockmass, a value for λ has been estimated via the combination of the Ground Reaction Curve (GRC) and the Longitudinal Displacement Profile (LDP), according to Carranza-Torres (2004) and Vlachopoulos and Diederichs (2009), respectively, with the assumptions of unsupported tunnel face and theoretically zero installation distance of the primary support from the tunnel face. For an incompetent rockmass, lower values of λ , in addition to the calculated ones, have been adopted in

the parametric study, due to the decreasing effect that typically implemented face treatment measures have on the level of deconfinement. On the contrary, for a competent rockmass, higher values of λ have also been investigated due to the prevailing practice of increasing the primary support installation distance from the tunnel face, resulting in increasing the degree of deconfinement.

The effect of deconfinement ratio λ is sufficiently summarized to its inversely proportional relation to the magnitude of the developing axial force, as expected, according to the theory of convergence-confinement. This response is constant for all the numerical analyses indicative steps, thus at different stages of the junction tunnel’s construction sequence.

Additionally, varying the deconfinement ratio λ does not influence the stress redistribution mechanism at the intersection area.

Figure 8 presents the effect of the size of the opening (diameter of the junction tunnel) on the tangential (N_θ) and the radial (N_R) axial force acting on the primary support at the periphery of the opening of the main tunnel at the left intersection area. Thus, the variable parameter is the ratio D/d and a set of indicative numerical analyses with specific values for σ_{cm}/p_o , K_o , H/D and λ , is presented.

The results indicate that increasing the size of the opening causes the development of higher maximum

Fig. 10 Distribution of the max and the min tangential (N_θ) axial force at the springline ($\Theta = 90^\circ$) and the crown ($\Theta = 360^\circ$) of the opening of the main tunnel at the left intersection area, for $K_o = 1$, $H/D = 6.7, 13.4$, $D/d = 1.2, 1.5, 2$, $\lambda = 0.5, 0.7$, relative to the modified geotechnical conditions ratio $(\sigma_{cm}/p_o)^{0.55} \cdot (H/D)^{0.45}$, for scenarios 3 and 4

(compressive) tangential and radial axial force, regardless of the assumed scenario. The minimum (compressive or tensile) radial axial force seems to be practically not affected by the size of the opening. On the contrary, the minimum tangential axial force is

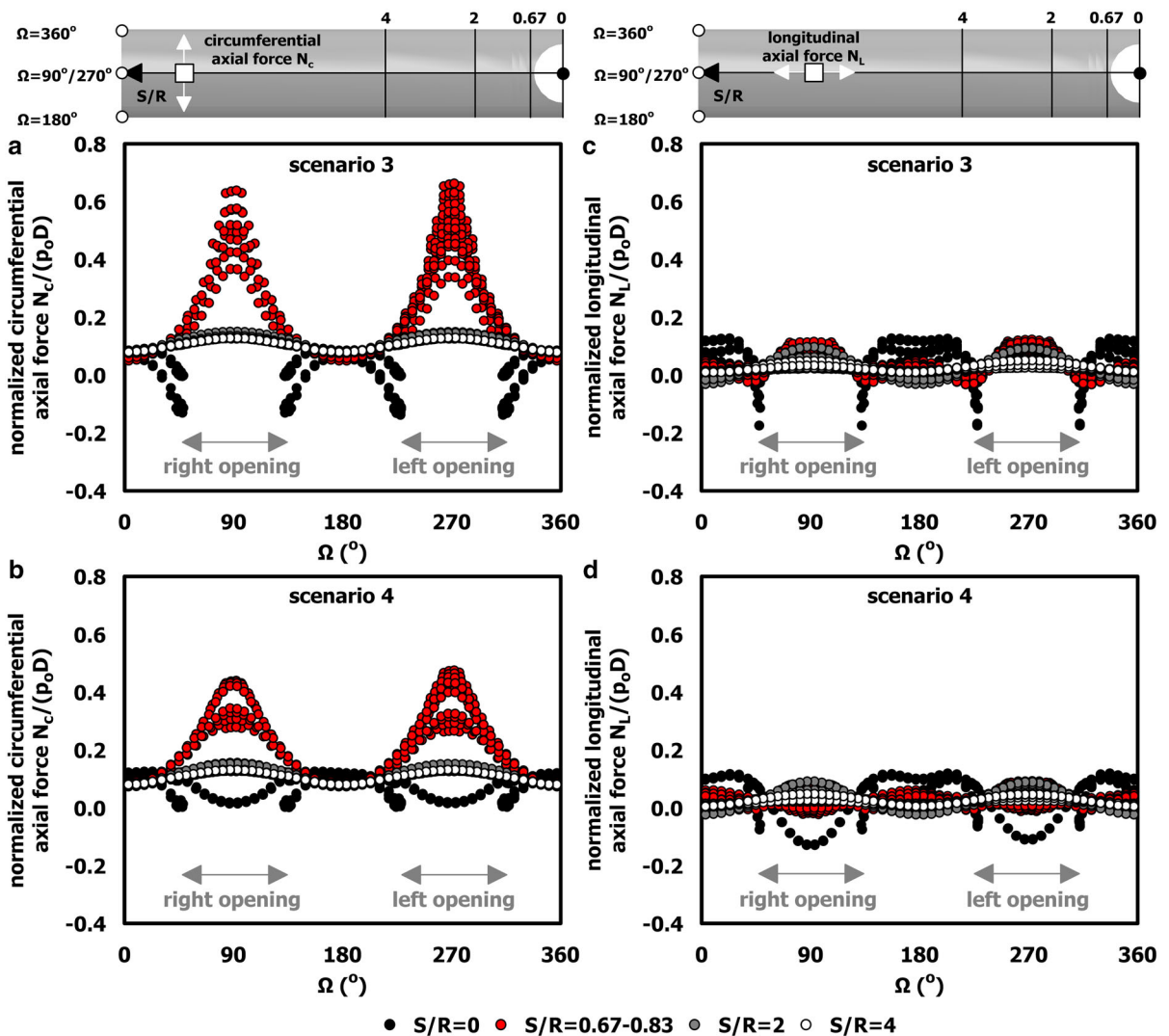
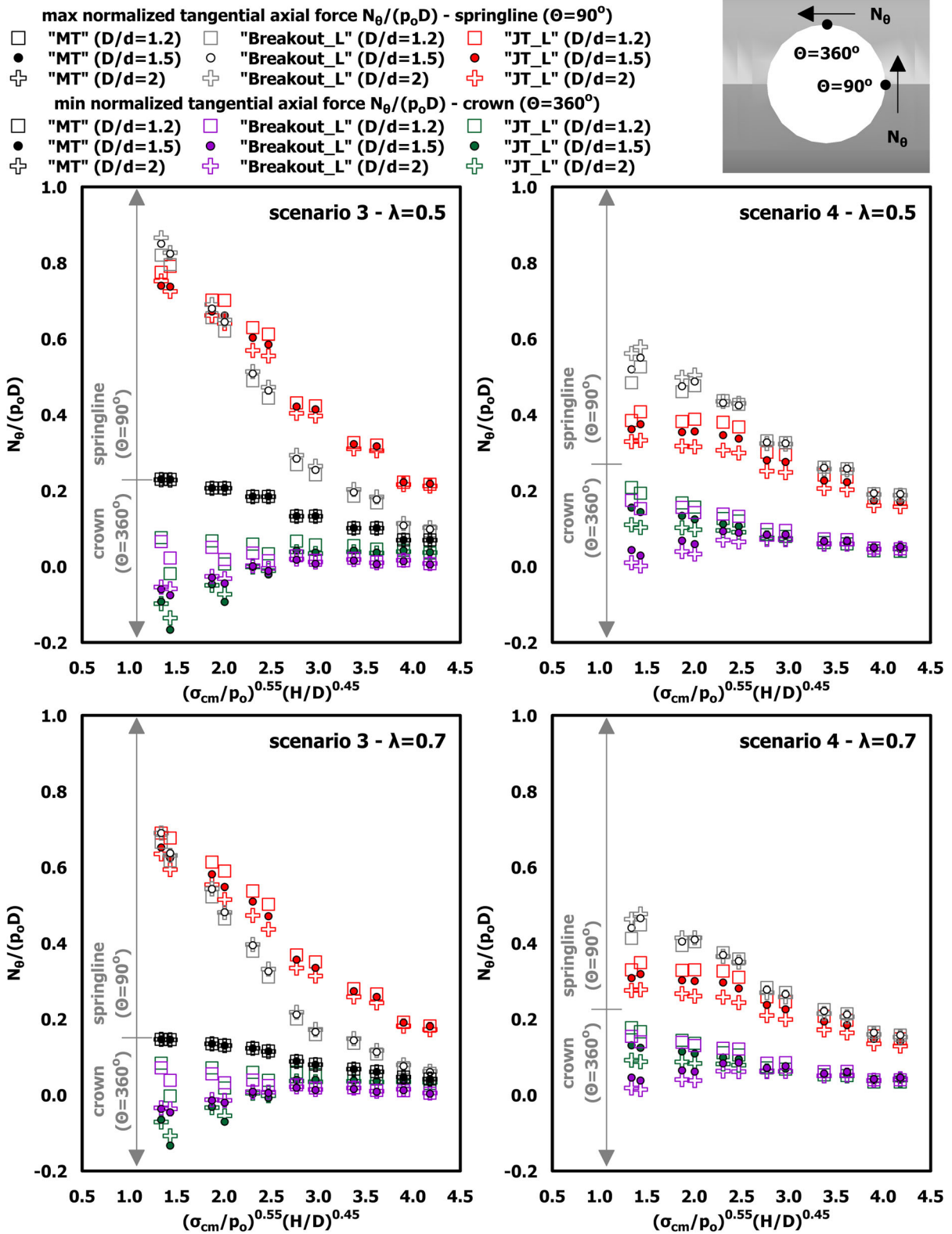
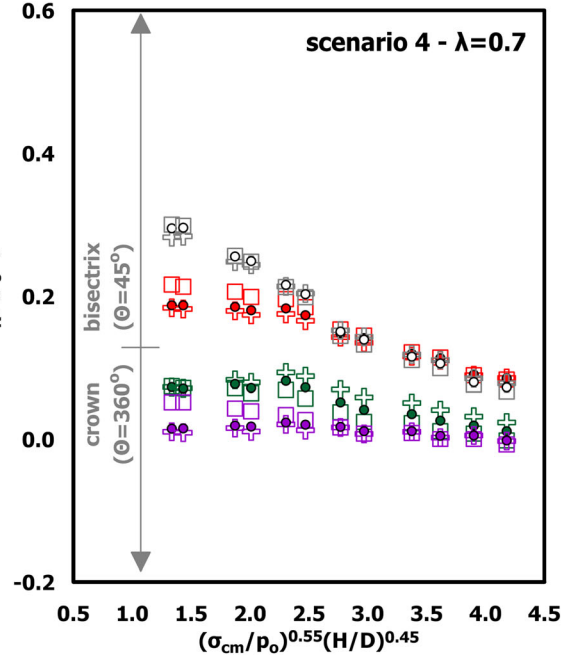
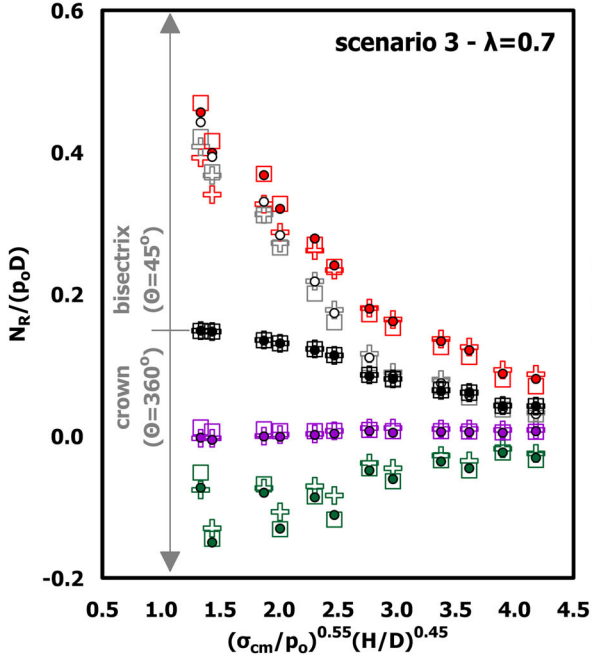
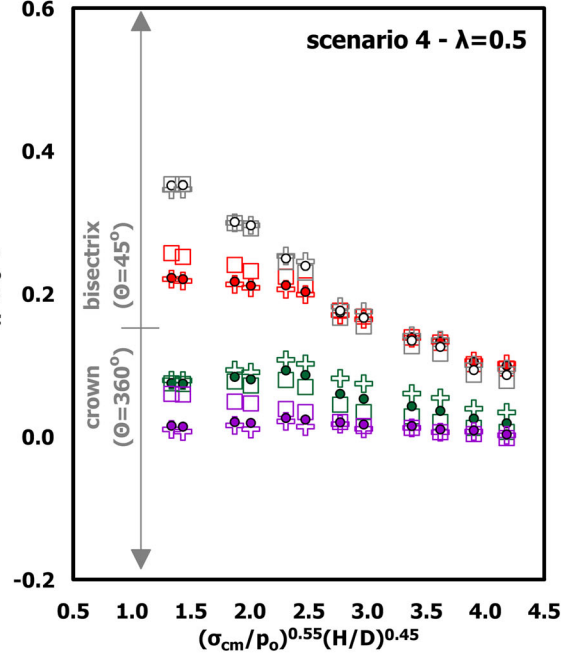
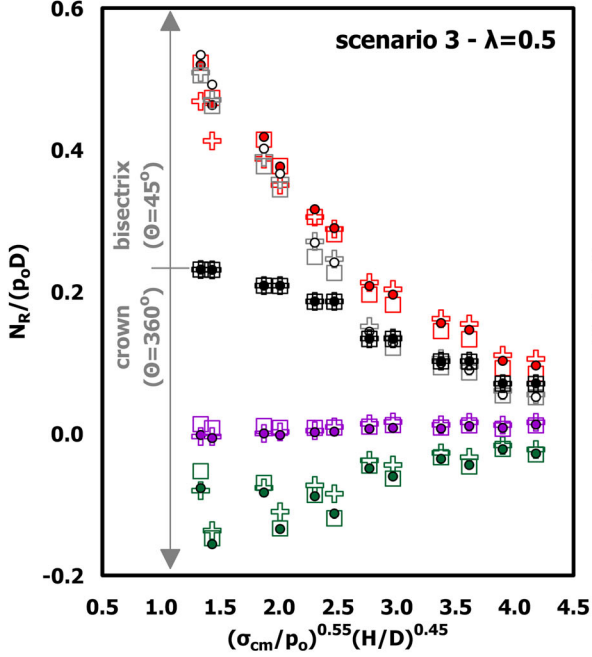
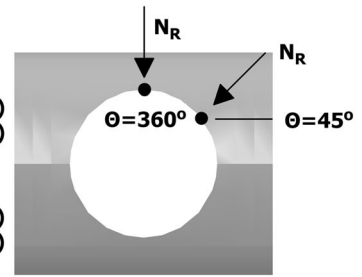


Fig. 9 Distribution of the circumferential (N_c) (a, b) and the longitudinal (N_L) (c, d) axial force at representative sections along the main tunnel, for scenarios 3 and 4 (Case: $\sigma_{cm}/p_o = 0.4$, $K_o = 0.5$, $H/D = 6.7$, $D/d = 1.5$, $\lambda = 0.7$)



- max normalized radial axial force $N_R/(p_o D)$ - bisectrix ($\Theta=45^\circ$)**
- "MT" (D/d=1.2) □ "Breakout_L" (D/d=1.2) □ "JT_L" (D/d=1.2)
 - "MT" (D/d=1.5) ○ "Breakout_L" (D/d=1.5) ● "JT_L" (D/d=1.5)
 - ⊕ "MT" (D/d=2) ⊕ "Breakout_L" (D/d=2) ⊕ "JT_L" (D/d=2)
- min normalized radial axial force $N_R/(p_o D)$ - crown ($\Theta=360^\circ$)**
- "MT" (D/d=1.2) □ "Breakout_L" (D/d=1.2) □ "JT_L" (D/d=1.2)
 - "MT" (D/d=1.5) ● "Breakout_L" (D/d=1.5) ● "JT_L" (D/d=1.5)
 - ⊕ "MT" (D/d=2) ⊕ "Breakout_L" (D/d=2) ⊕ "JT_L" (D/d=2)



◀ **Fig. 11** Distribution of the max and the min radial (N_R) axial force at the bisectrix ($\Theta = 45^\circ$) and the crown ($\Theta = 360^\circ$) of the opening of the main tunnel at the left intersection area, for $K_o = 1$, $H/D = 6.7, 13.4$, $D/d = 1.2, 1.5, 2$, $\lambda = 0.5, 0.7$, relative to the modified geotechnical conditions ratio $(\sigma_{cm}/p_o)^{0.55} \cdot (H/D)^{0.45}$, for scenarios 3 and 4

influenced and varies from compressive to tensile according to the adopted scenario. Specifically, increasing the junction tunnel's diameter leads to either decreasing the tension amplitude or preventing tension development entirely. This response develops in a more intense degree for scenario 4, compared to scenario 3.

4.3 Axial Forces Along the Main Tunnel—Extent of the Influence Zone

Figure 9 presents the distribution of the circumferential (N_c) (Fig. 9a, b) and the longitudinal (N_L) (Fig. 9c, d) axial force at representative sections of the main tunnel for scenarios 3 (Fig. 9a, c) and 4 (Fig. 9b, d). For each section, the results are illustrated with a different color. The normalized longitudinal distance of the selected sections from the center of the intersection is $S/R = 0$ (black color), 0.67 – 0.83 (red), 2 (grey) and 4 (white), respectively. The results for every individual section include the induced axial forces acting on the primary support for all the indicative steps (“MT”, “Breakout_L”, “JT_L”, “Breakout_R”, “JT_R”). Precisely, the distribution of the axial forces is presented along “unwrapped” sections of the main tunnel, where each position of its periphery is determined via the angle Ω , as defined in Fig. 2e. Therefore, the left opening is oriented for $\Omega = 225^\circ$ – 315° , while the right for $\Omega = 45^\circ$ – 135° , respectively.

The results evaluate the loading mechanism presented in Figs. 3 and 5 additionally indicate that the stress state of the left opening, which is precedent in both scenarios, is slightly more intense compared to the right one, regardless of the assumed construction sequence. For this reason, only the results for the left intersection area are presented within this paper. Another conclusion derived from Fig. 9 is the range of the zone along the main tunnel influenced due to the construction of the junction tunnel and therefore requiring strengthening of the primary support system. The extent of the zone is approximately two diameters

(2D) of the main tunnel measuring from the center of the intersection, with criterion the distance where the variation of the axial forces is reducing at negligible levels.

The calculated extent of the influence zone is among the range of other proposed values such as $1d$ (Spyridis and Bergmeister 2015), $1.6B$ – $2.4B$ (Li et al. 2016) and $2.5D$ (Liu et al. 2009). The deviations from these researches are due to the different assumptions or numerical modeling techniques. For instance, Spyridis and Bergmeister (2015) conduct elastic parametric numerical analyses for shallow tunnel junctions, simulate the construction of the main tunnel in a single step without precedent deconfinement and model only the breakout (creation of the opening). Respectively, Liu et al. (2009) utilize elastoplastic numerical analyses, assuming a step-by-step construction sequence, for a case study of non-circular shallow intersecting tunnels, where the arching effect of the surrounding geomaterial is not fully developing.

4.4 Design Charts

Figure 10 presents the maximum and the minimum tangential (N_θ) axial force at the springline ($\Theta = 90^\circ$) and the crown ($\Theta = 360^\circ$) of the opening of the main tunnel at the left intersection area, versus key geomaterial and geometry parameters. Respectively, Fig. 11 presents the maximum and the minimum radial (N_R) axial force at the bisectrix (location with $\Theta = 45^\circ$) and the crown ($\Theta = 360^\circ$) of the opening of the main tunnel at the left intersection area. The results are presented for different values of H/D , D/d , and λ , relative to the modified geotechnical conditions ratio $(\sigma_{cm}/p_o)^{0.55} (H/D)^{0.45}$, for scenarios 3 and 4. This parameter is a modified ratio resembling the geotechnical conditions and is utilized to incorporate the effect of the overburden height ratio (H/D) on the geotechnical conditions ratio (σ_{cm}/p_o). In this context, Figs. 12 and 13 present the corresponding results for different values of K_o , H/D , and λ .

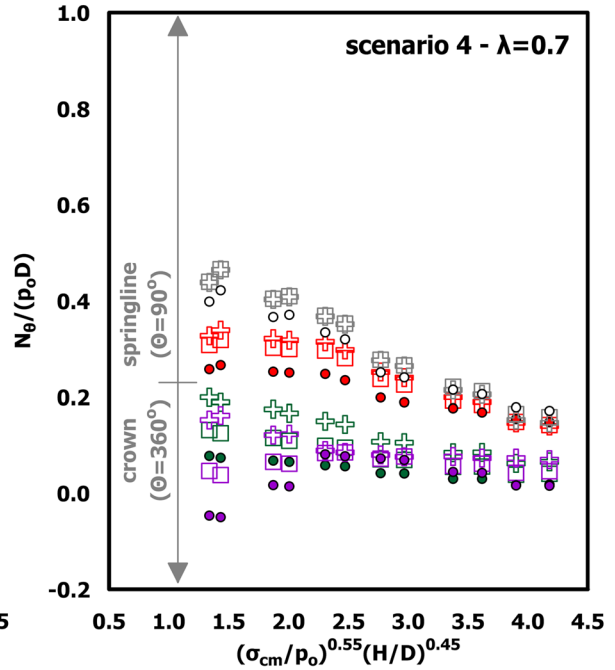
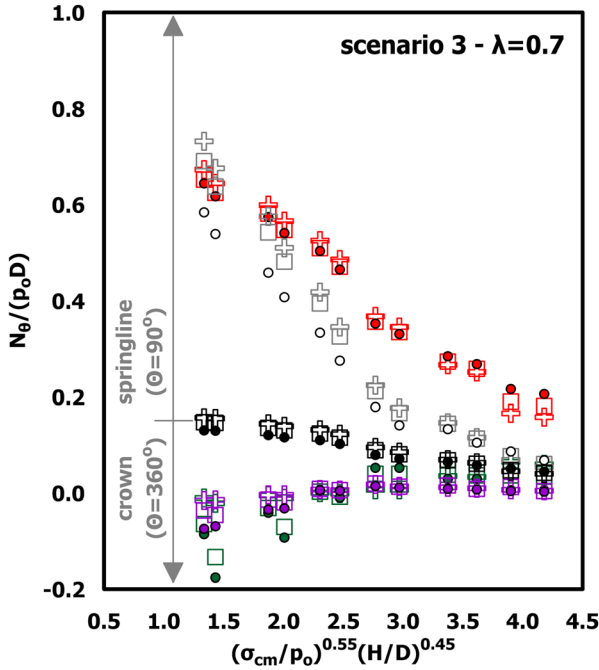
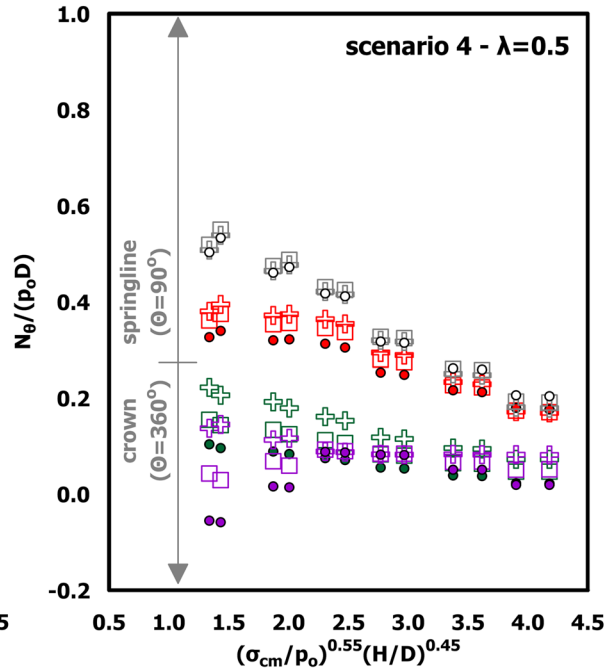
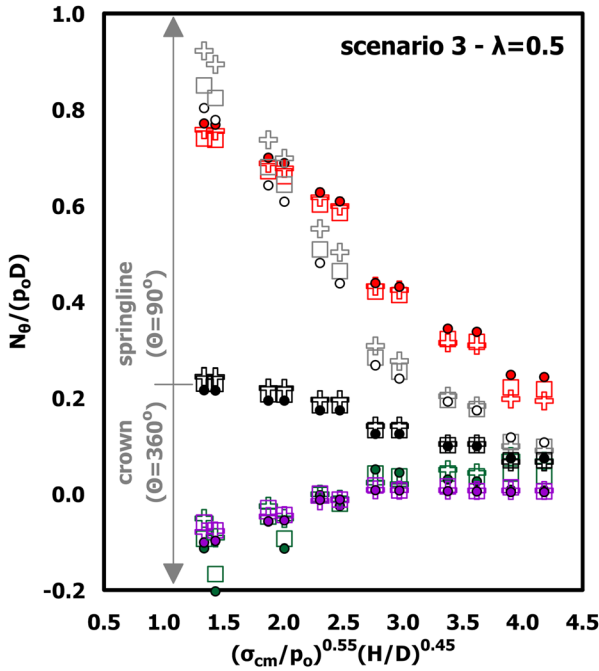
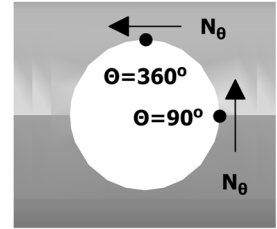
The graphs present the results for the steps “MT”, “Breakout_L” and “JT_L” at the left intersection area, while the corresponding results for the steps “Breakout_R” and “JT_R” are not included in the plots to facilitate clarity. However, the latter can be estimated as follows: i. by using the results of the step “JT_L” for scenario 3 and the step “Breakout_L” for scenario 4, respectively, for the minimum

max normalized tangential axial force $N_\theta/(p_oD)$ - springline ($\theta=90^\circ$)

- "MT" ($K_o=0.5$) ○ "Breakout_L" ($K_o=0.5$) ● "JT_L" ($K_o=0.5$)
- "MT" ($K_o=1$) □ "Breakout_L" ($K_o=1$) □ "JT_L" ($K_o=1$)
- + "MT" ($K_o=1.5$) + "Breakout_L" ($K_o=1.5$) + "JT_L" ($K_o=1.5$)

min normalized tangential axial force $N_\theta/(p_oD)$ - crown ($\theta=360^\circ$)

- "MT" ($K_o=0.5$) ● "Breakout_L" ($K_o=0.5$) ● "JT_L" ($K_o=0.5$)
- "MT" ($K_o=1$) □ "Breakout_L" ($K_o=1$) □ "JT_L" ($K_o=1$)
- + "MT" ($K_o=1.5$) + "Breakout_L" ($K_o=1.5$) + "JT_L" ($K_o=1.5$)



◀ **Fig. 12** Distribution of the max and the min tangential (N_{θ}) axial force at the springline ($\Theta = 90^\circ$) and the crown ($\Theta = 360^\circ$) of the opening of the main tunnel at the left intersection area, for $K_o = 0.5, 1, 1.5$, $H/D = 6.7, 13.4$, $D/d = 1.5$, $\lambda = 0.5, 0.7$, relative to the modified geotechnical conditions ratio $(\sigma_{cm}/p_o)^{0.55} \cdot (H/D)^{0.45}$, for scenarios 3 and 4

(compressive or tensile) axial forces without any modification, ii. by increasing by 10–20% the results of these steps for the maximum (compressive) axial forces. These recommendations are suggested by the output presented in Figs. 3, 5. The results for the right intersection area are also deliberately not presented, since, as already shown in Fig. 9, the results for the left one are slightly more adverse and, hence, these results could be utilized for the design of both intersection areas. Therefore, Figs. 10, 11, 12 and 13 can be utilized as general-purpose design charts for the preliminary estimation of primary support requirements at tunnel junctions since they provide the critical values (envelope) of the developing axial forces in the tangential and the radial direction at the periphery of the opening for both intersection areas.

The results, presented in Figs. 10, 11, 12 and 13, indicate that the prevailing geotechnical conditions significantly affect the induced axial forces. Specifically, their worsening leads to higher values of the maximum (compressive) tangential and radial axial forces, emerging the potential demand for increased capacity of the primary support measures, for instance, by thickening the shotcrete layer at the extent of the influence zone. Furthermore, specific measures could be required to prevent tensile cracking or failure of the primary support system at the crown/invert area, especially if the geotechnical conditions deteriorate.

Another parameter that has a critical role in the magnitude and the sign of the induced axial forces is the assumed construction sequence of the junction tunnel. It can be concluded that scenario 3 is generally more adverse than scenario 4, since, at the latter, the compressive stress regime is comparatively lower, while the tensile stress regime practically does not develop. The effect of the scenario on the developing stress regimes should be considered with the horizontal stress ratio (K_o) and the size of the opening (d) since it exhibits correlation/interaction with these parameters.

The horizontal stress ratio influences the magnitude of the maximum tangential and radial axial forces; the higher values of K_o lead to higher loading at the primary support, in both scenarios. Also, regarding the minimum tangential and radial axial forces, the higher values of K_o generally control or prevent the development of tension, with this phenomenon being more intense in scenario 4, rather than scenario 3.

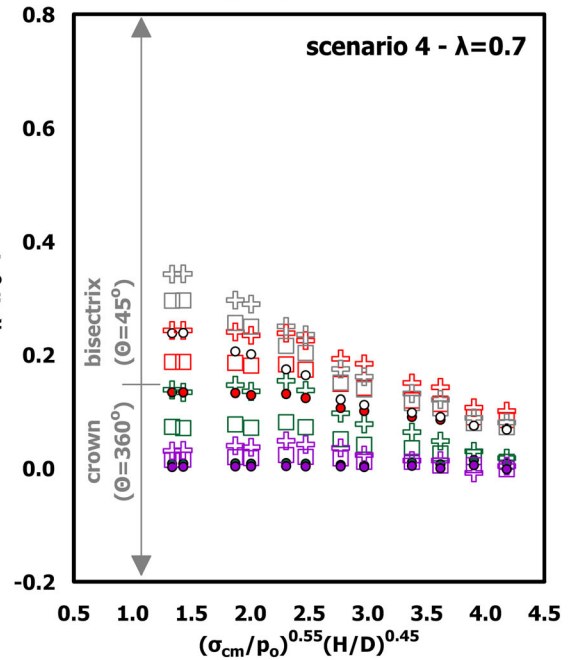
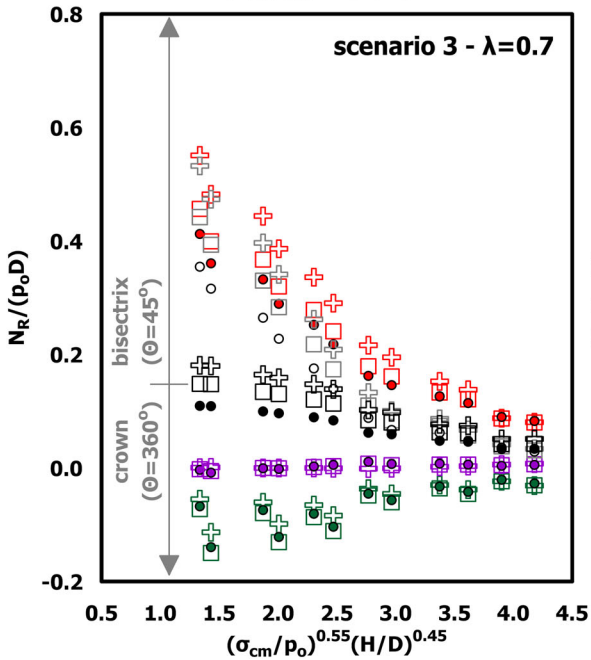
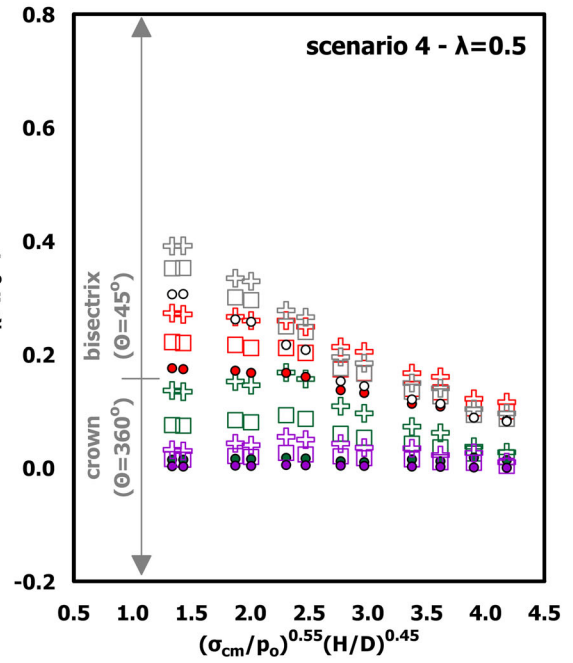
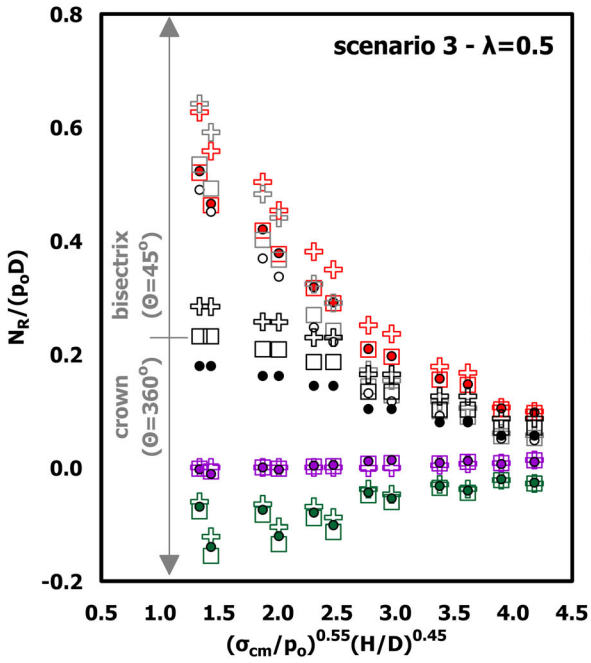
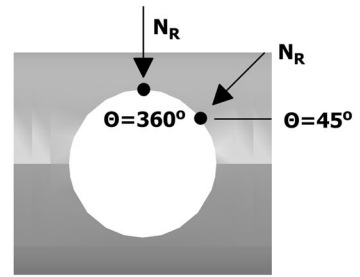
The increase of the diameter of the junction tunnel (decrease of D/d) generally tends to enhance the maximum tangential and radial axial forces, except for some diversifications emerging for challenging or poor “squeezing” geotechnical conditions, in both scenarios. Furthermore, the increase contributes to reducing or eliminating the tensile level of the minimum tangential and radial axial forces, depending though on the adopted construction sequence. The latter effect is amplified in scenario 4, instead of scenario 3.

4.5 Reduction Factors of the Tangential Axial Force Along the Springline of the Main Tunnel

The tangential axial force (N_{θ}) along the left springline ($\Omega = 90^\circ$) of the main tunnel decreases as the normalized (horizontal) distance (Y/r) from the boundary of the springline ($\Theta = 90^\circ$) of the opening increases, as shown in Fig. 9. A reduction factor is utilized to quantify its net decrease at locations with ascending normalized (horizontal) distance (Y/r). Thus, the reduction factor is the ratio of the axial force at a location with $Y/r > 0$, versus the axial force acting on the boundary of the opening, where $Y/r = 0$.

Figure 14 presents the average reduction factors (calculated/weighted for the whole construction sequence of the junction tunnel), relative to $(\sigma_{cm}/p_o)^{0.55} \cdot (H/D)^{0.45}$, for a constant value of K_o , and different values of H/D , D/d , and λ , thus, incorporating most of the parametrically examined variables, for scenario 3. For scenario 4, the reduction factors are not calculated, since it is compared to scenario 3, favorable, as already discussed. The results corresponding to different values of the deconfinement ratio (λ) of the main tunnel and the overburden height ratio (H/D) are distinguished by utilizing different symbols. Furthermore, the processing/interpretation of the results is facilitated with the aid of different colors.

- max normalized radial axial force $N_R/(p_o D)$ - bisectrix ($\theta=45^\circ$)**
- "MT" ($K_o=0.5$) ○ "Breakout_L" ($K_o=0.5$) ● "JT_L" ($K_o=0.5$)
 - "MT" ($K_o=1$) □ "Breakout_L" ($K_o=1$) □ "JT_L" ($K_o=1$)
 - ⊕ "MT" ($K_o=1.5$) ⊕ "Breakout_L" ($K_o=1.5$) ⊕ "JT_L" ($K_o=1.5$)
- min normalized radial axial force $N_R/(p_o D)$ - crown ($\theta=360^\circ$)**
- "MT" ($K_o=0.5$) ● "Breakout_L" ($K_o=0.5$) ● "JT_L" ($K_o=0.5$)
 - "MT" ($K_o=1$) □ "Breakout_L" ($K_o=1$) □ "JT_L" ($K_o=1$)
 - ⊕ "MT" ($K_o=1.5$) ⊕ "Breakout_L" ($K_o=1.5$) ⊕ "JT_L" ($K_o=1.5$)



◀ **Fig. 13** Distribution of the max and the min radial (N_R) axial force at the bisectrix ($\Theta = 45^\circ$) and the crown ($\Theta = 360^\circ$) of the opening of the main tunnel at the left intersection area, for $K_o = 0.5, 1, 1.5, H/D = 6.7, 13.4, D/d = 1.5, \lambda = 0.5, 0.7$, relative to the modified geotechnical conditions ratio $(\sigma_{cm}/p_o)^{0.55} \cdot (H/D)^{0.45}$, for scenarios 3 and 4

The results indicate, via a macroscopic assessment, that the examined parameters ($H/D, D/d, \lambda, \sigma_{cm}/p_o$) do not have a crucial effect on the distribution of the reduction factors. The distance from the boundary of the opening (Y/r) along the springline, primarily, and the size of the opening (d), secondarily, are the parameters influencing more the magnitude of the reduction factors. The results show that the tangential axial force significantly decreases at close distances from the boundary of the opening. Specifically, at a distance $Y/D = 0.1-0.2$ away from the boundary of the opening, the tangential axial force reduces by half. This response suggests that a factored value of the maximum tangential axial force, developing at the

boundary of the springline of the opening, can be utilized as a design value for the intersection area.

Implementing such a procedure in the design of tunnel junctions does not sacrifice the stability of the intersection area since it takes into account the auxiliary effect of the typically applied strengthening measures at the intersection zone. Indicatively, strengthening measures, such as thickening of the shotcrete layer, installation of steel sets, use of anchorages and construction of a stiff concrete slab (“collar”) at the periphery of the opening, significantly enhance the capacity of the primary support measures and prevent local compressive failures. Furthermore, this philosophy in the design of tunnel junctions allows potential limited/local yielding of the primary support (if the loads exceed its capacity) at the springlines. It assumes that the additional loads are adequately undertaken via stress redistribution in the vicinity of the vulnerable areas; such a mechanical response of the temporary support measures can be approved, during the construction of the junction tunnel, if the yielding/redistribution phenomena are prevented from uncontrollably expanding. These

reduction factors of the tangential axial force (N_θ) along the left springline ($\Omega=90^\circ$) of the main tunnel, relative to the normalized (horizontal) distance (Y/r) from the boundary of the springline ($\Theta=90^\circ$) of the opening

- ($\lambda=0.5 - H/D=6.7$) □ ($\lambda=0.6 - H/D=6.7$) ⊕ ($\lambda=0.7 - H/D=6.7$)
- ◇ ($\lambda=0.5 - H/D=13.4$) ⊗ ($\lambda=0.6 - H/D=13.4$) ⊛ ($\lambda=0.7 - H/D=13.4$)

symbol color - distance (Y/r)

$D/d=1.2$: $Y/r=0.13$ - $Y/r=0.20$ - $Y/r=0.30$ - $Y/r=0.40$

$D/d=1.5$: $Y/r=0.13$ - $Y/r=0.19$ - $Y/r=0.25$ - $Y/r=0.38$ - $Y/r=0.50$

$D/d=2$: $Y/r=0.13$ - $Y/r=0.20$ - $Y/r=0.27$ - $Y/r=0.34$ - $Y/r=0.50$

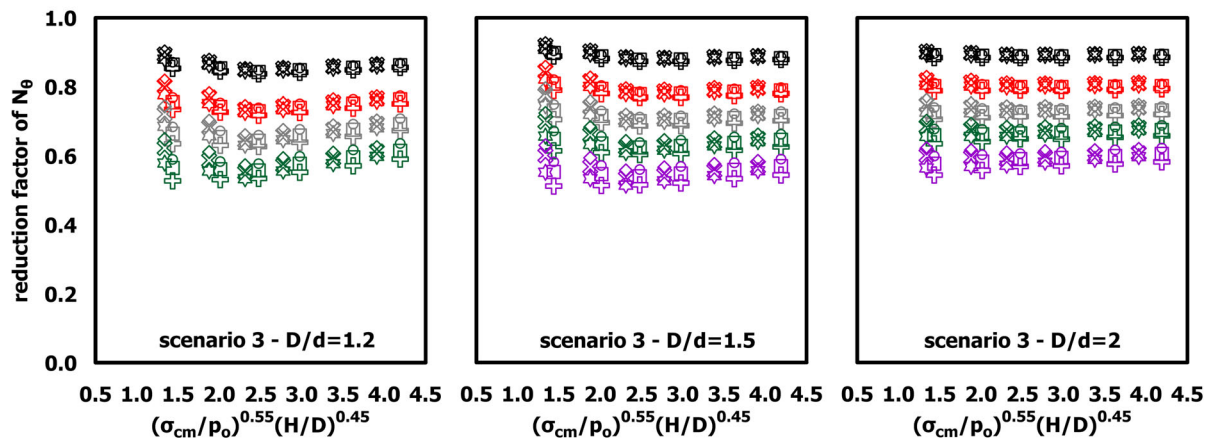
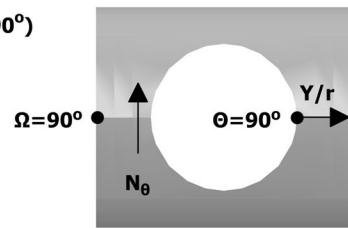


Fig. 14 Distribution of the reduction factors of the tangential axial force (N_θ) along the left springline ($\Omega = 90^\circ$) of the main tunnel, for $K_o = 1, H/D = 6.7, 13.4, D/d = 1.2, 1.5, 2, \lambda = 0.5,$

$0.6, 0.7$, relative to the modified geotechnical conditions ratio $(\sigma_{cm}/p_o)^{0.55} \cdot (H/D)^{0.45}$, for scenario 3

assumptions suggest that a safety factor marginally being equal to 1 for a limited region of the intersection zone, oriented in the proximity of the boundary of the opening, can be adopted since the design is not for the permanent lining. Hence, the proposed reduction factors presented in Fig. 14 provide a spectrum with different levels for the percentage decrease of the tangential axial force (incorporating a different level of risk), applicable for designing either the left or the right intersection area of a tunnel junction, which should be critically used by assessing the unique conditions of each specific tunneling project.

5 Conclusions

This paper utilizes parametric 3D Finite Element analyses to calculate the distribution of the axial forces at the junction of deep, circular tunnels, where a junction tunnel intersects an existing main tunnel perpendicularly. Several relevant parameters, as shown in Table 1, are varied to produce dimensionless graphs of the axial forces developing on the primary support at the junction area. The results of the analyses indicate that the influence zone extends to approximately two diameters (2D) of the main tunnel at either side from the center of the intersection. Beyond this zone, the interaction effects are practically eliminated.

The results of the analyses are presented at the quarter of the periphery of the opening ($\Theta = 0^\circ\text{--}90^\circ$) of the main tunnel, due to the symmetry in geometry and loading conditions. This area splits into two distinct regions. In region $\Theta = 30^\circ\text{--}90^\circ$, significant additional compressive loading develops. The maximum (compressive) tangential (N_θ) and radial (N_R) axial forces occur at the springline of the opening ($\Theta = 90^\circ$) and the bisectrix of the quarter of the opening (location with $\Theta = 45^\circ$), respectively. In region $\Theta = 0^\circ\text{--}30^\circ$, either compressive unloading and tensile loading or compressive and tensile loading develop, depending on the construction sequence of the junction tunnel (inward or outward excavation). The minimum (compressive or tensile) tangential (N_θ) and radial (N_R) axial forces occur at the crown of the opening ($\Theta = 0^\circ$). This categorization of the stress regions can be adopted as a general pattern and is independent of the parametrically examined variable parameters.

The construction sequence of the junction tunnels is investigated via four alternative scenarios and proves to be a crucial parameter for the stress state at the intersection area. More adverse loading conditions occur when the junction tunnel moves away (starts) from the main tunnel, compared to when the junction tunnel moves towards (ends up at) the main tunnel. In the first case, higher compression and tension develop, while in the second case, compression is lower and tension is practically negligible. Therefore, increasing the capacity of the primary support within the extent of the influence zone could be required to prevent either tensile cracking/failure at the crown/invert areas or compressive failure (due to local overstress) at the springline areas of the opening, depending on the geomaterial's strength and the tunnel depth.

The diameter of the junction tunnel (d), the horizontal stress ratio (K_0), the degree of deconfinement (λ) of the main tunnel and the rockmass strength (σ_{cm}) influence the magnitude of the induced axial forces in the intersection zone. Although these parameters do not significantly affect the pattern of the enhanced compressive stress region, they have a significant effect on the region of mixed loading regime (compressive and tensile). Precisely, increasing K_0 or the size of the opening (d) reduces or eliminates the tensile loading regime at the periphery of the opening, with this effect depending on the construction scenario (inward or outward excavation of the junction tunnel).

The normalized graphs of the calculated distributions of the axial forces at the intersection area can be used as general-purpose design charts for the preliminary estimation of primary support requirements at tunnel junctions. Furthermore, the simulation of different scenarios, including the simultaneous or in sequence construction of the junction tunnel's branches, advancing either inwards or outwards to the main tunnel, makes these design charts applicable for a wide range of junction configurations (cross "+", "T" and "H").

References

- Brown ET, Hocking G (1976) Use of the three dimensional boundary integral equation method for determining stresses at tunnel intersections

- Carranza-Torres C (2004) Elasto-plastic solution of tunnel problems using the generalized form of the Hoek-Brown failure criterion. *Int J Rock Mech Min Sci*. <https://doi.org/10.1016/j.ijrmmms.2004.03.111>
- Förder M, Abel F, Tirpitz ER (2008) The Malmö Citytunnel, Sweden—tunnelling in Scandinavia. *Beton Stahlbetonbau* 103:689–697
- Gerçek H (1986) Stability considerations for underground excavation intersections. *Min Sci Technol*. [https://doi.org/10.1016/S0167-9031\(86\)90194-5](https://doi.org/10.1016/S0167-9031(86)90194-5)
- Hocking G (1978) Stresses around tunnel intersections. In: computer methods in tunnel design, conference proceedings. Thomas Telford Publishing, pp. 41–60. <https://doi.org/10.1680/cmitd.00568.0003>
- Hoek E, Brown ET (2019) The Hoek-Brown failure criterion and GSI—2018 edition. *J Rock Mech Geotech Eng*. <https://doi.org/10.1016/j.jrmge.2018.08.001>
- Hoek E, Diederichs MS (2006) Empirical estimation of rock mass modulus. *Int J Rock Mech Min Sci*. <https://doi.org/10.1016/j.ijrmmms.2005.06.005>
- Hsiao FY, Wang CL, Chern JC (2009) Numerical simulation of rock deformation for support design in tunnel intersection area. *Tunn Undergr Sp Technol*. <https://doi.org/10.1016/j.tust.2008.01.003>
- Hsiao FY, Yu CW, Chern JC (2005) Modeling the behaviors of the tunnel intersection areas adjacent to the ventilation shafts in the Hsuehshan tunnel. In: Proceedings of the international symposium on design, construction and operation of long tunnels, Taipei
- Insam R, Wahlen R, Wieland G (2019) Brenner base tunnel—interaction between underground structures, complex challenges and strategies. In: Tunnels and underground cities: engineering and innovation meet archaeology, architecture and art—proceedings of the wtc 2019 ita-aites world tunnel congress. <https://doi.org/10.1201/9780429424441-408>
- Jones BD (2007) Stresses in sprayed concrete tunnel junctions. Doctoral thesis, University of Southampton
- Kalos A, Kavvas M (2017) A constitutive model for strain-controlled strength degradation of rockmasses (SDR). *Rock Mech Rock Eng*. <https://doi.org/10.1007/s00603-017-1288-x>
- Ke W, Shuaishuai C, Qianjin Z, Zheng Z, Jiahui Z, Yalin Y (2019) Mechanical mechanism analysis and influencing factors of subway cross passage construction. *Lat Am J Solids Struct*. <https://doi.org/10.1590/1679-78255512>
- Li Y, Jin X, Lv Z, Dong J, Guo J (2016) Deformation and mechanical characteristics of tunnel lining in tunnel intersection between subway station tunnel and construction tunnel. *Tunn Undergr Sp Technol*. <https://doi.org/10.1016/j.tust.2016.02.016>
- Liu HL, Li SC, Li LP, Zhang QQ (2017) Study on deformation behavior at intersection of adit and major tunnel in railway. *KSCE J Civ Eng*. <https://doi.org/10.1007/s12205-017-2128-y>
- Liu HY, Small JC, Carter JP, Williams DJ (2009) Effects of tunnelling on existing support systems of perpendicularly crossing tunnels. *Geotech Comput*. <https://doi.org/10.1016/j.compgeo.2009.01.013>
- Marinos P, Hoek E (2018) GSI: a geologically friendly tool for rock mass strength estimation. In: ISRM international symposium 2000, IS 2000
- Pant B (1971) Analysis and design of pressure tunnel intersection. Indian Society of Engineering Geology, Tunnelling Seminar, Part I
- Pöttler R (1992) Three-dimensional modelling of junctions at the channel tunnel project. *J Numer Anal Methods Geomech Int*. <https://doi.org/10.1002/nag.1610160906>
- Riley FW (1964) Stress at tunnel intersections. *J Eng Mech Div* 90(2):167–180
- Schikora K, Piegendorfer M, Filus M (2013) Plane and three-dimensional analysis in tunneling using the example of current and planned construction. *Beton Stahlbetonbau* 108:252–263
- Sjöberg J, Leander M, Saiang D (2006) Three-dimensional analysis of tunnel intersections for a train tunnel under Stockholm. In: Proceedings of the North American Tunneling 2006 Conference
- Spyridis P, Bergmeister K (2015) Analysis of lateral openings in tunnel linings. *Tunn Undergr Sp Technol*. <https://doi.org/10.1016/j.tust.2015.08.005>
- Swoboda G, Shen XP, Rosas L (1998) Damage model for jointed rock mass and its application to tunnelling. *Comput Geotech*. [https://doi.org/10.1016/S0266-352X\(98\)00009-3](https://doi.org/10.1016/S0266-352X(98)00009-3)
- Tsuchiyama S, Hayakawa M, Shinokawa T, Konno H (1988) Deformation behavior of the tunnel under the excavation of crossing tunnel. numerical methods of geomechanics. Balkema, Rotterdam, pp 1591–1596
- Vlachopoulos N, Diederichs MS (2009) Improved longitudinal displacement profiles for convergence confinement analysis of deep tunnels. *Rock Mech Rock Eng*. <https://doi.org/10.1007/s00603-009-0176-4>

Publisher's Note Springer Nature remains neutral with regard to jurisdictional claims in published maps and institutional affiliations.